

**DYNAMIC TERRAIN FOLLOWING: NVCPD SCANNING
TECHNIQUE IMPROVEMENT**

A Thesis
Presented to
The Academic Faculty

by

YURY PYEKH

In Partial Fulfillment
of the Requirements for the Degree
Master of Science in Mechanical Engineering

Georgia Institute of Technology
August 2010

**DYNAMIC TERRAIN FOLLOWING: NVCPD SCANNING
TECHNIQUE IMPROVEMENT**

Approved by:

Dr. Steven Danyluk, Advisor
School of Mechanical Engineering
Georgia Institute of Technology

Dr. Rhett Mayor
School of Mechanical Engineering
Georgia Institute of Technology

Dr. Levent Degertekin
School of Mechanical Engineering
Georgia Institute of Technology

Date Approved: May 7, 2010

ACKNOWLEDGEMENTS

First, I would especially like to acknowledge my advisor, Dr. Steven Danyluk, whose guidance and experience have made this thesis possible. I would like to thank Dr. Rhett Mayor, Dr. Levent Degertekin for serving in the defense committee.

I would like to thank all the members of our research group that helped me. I would like to express my gratitude to Dr. Zharin and Sergey Tereshko for the input and knowledge share in designing and develop probes. Thanks to Andres, Daniel, Dr. Yang, Fang, Frank, Travis, Vicky, for their help, advices, and for creating a great working atmosphere.

I would like to recognize all my friends for their contribution. Without their moral and economical support it would be much harder to accomplish this work.

Finally, I would like to express special thanks to my family for all the support they have given to me. I would like to thank my brother for his help, support and encouragement through my life. I am very grateful to my wife for her patience and faith. Thanks to my little son for keeping me awake and motivated.

TABLE OF CONTENTS

	Page
ACKNOWLEDGEMENTS	iii
LIST OF TABLES	vi
LIST OF FIGURES	vii
LIST OF SYMBOLS AND ABBREVIATIONS	x
SUMMARY	xii
<u>CHAPTER</u>	
1 INTRODUCTION	1
2 BACKGROUND	3
Work Function	3
Contact Potential Difference	4
Kelvin Probe	6
Non-Vibrating CPD	9
General form of the nvCPD response	12
nvCPD response of a round probe tip	15
Effect of Fringe Fields on nvCPD Response Model	18
Typical nvCPD scanning setup and difficulties	22
Experimental Plan	25
3 EXPERIMENTAL DETAILS	27
Overall System Architecture	27
Hardware	28
Software	42
4 EXPERIMENTAL PROCEDURE	51

System Preparation	51
Scanning Technique	60
5 RESULTS AND DISCUSSION	64
6 CONCLUSION	80
APPENDIX A	82
APPENDIX B	87
REFERENCES	90

LIST OF TABLES

	Page
Table 3.1: Measurements specifications for fiber optic probe modules.	35
Table 3.2: Common and arbitrary waveform characteristics Agilent 33220A	38
Table 3.3: Components of the CPD sensor circuit.	42
Table 4.1: Typical data acquisition parameters.	59
Table 5.1: Goodness of fit.	66
Table A.1: ELMO HAR-5/60 general specification.	82
Table A.2: AS510/1 general specification.	83

LIST OF FIGURES

	Page
Figure 2.1: Schematic diagram of the work function and Fermi energy of a solid.	3
Figure 2.2: Schematic of contact potential difference.	5
Figure 2.3: Schematic of Vibrating CPD probe.	7
Figure 2.4: Schematic of Non-Vibrating CPD probe.	9
Figure 2.5: Schematic of the nvCPD probe passing over a surface: a) work function variation, b) topography variation, (c).combination of (a) and (b).	10
Figure 2.6: Schematic of a) the probe tip movement over a surface and b) expected nvCPD probe output for a given work function variation.	12
Figure 2.7: Schematic of round nvCPD probe tip translating over a surface with a feature.	15
Figure 2.8: Geometry of nvCPD probe passing the boundary of the feature.	16
Figure 2.9: Schematic of the electrical fields for an ideal (a) and a real (b) capacitor.	19
Figure 2.10: Schematic of the nvCPD response for an ideal (a) and a real (b) case.	20
Figure 2.11: Typical nvCPD scanning system.	23
Figure 2.12: Difficulties during the measurement process: incline, wobbling, non-planar surface.	24
Figure 2.13: Modified nvCPD Scanning technique.	25
Figure 2.14: Experimental Plan.	26
Figure 3.1: Photograph of Experimental Setup.	28
Figure 3.2: Schematic diagram of the system.	28
Figure 3.3: XYZ-positioning system	30
Figure 3.4: Schematic diagram of position system components.	31
Figure 3.5: Block diagram of position system.	31
Figure 3.6: Fiber Optic Probe Principle.	32

Figure 3.7: Sensor reflected light, close to target.	33
Figure 3.8: Maximum reflected light from Fiber Optic Sensor.	33
Figure 3.9: Typical Fiber Optic Probe response curve.	34
Figure 3.10: Waveform generator Agilent 33220A.	37
Figure 3.11: Voice Coil Actuator NCM02-17-035-2FE01.	39
Figure 3.12: Closed Loop VCA operating diagram.	39
Figure 3.13: a) Elmo HAR -5/60-1 drive; b) AS510 translation module.	40
Figure 3.14: Circuit diagram of CPD sensor.	41
Figure 3.15: CPD sensor photograph.	42
Figure 3.16: Schematic diagram of the Labview application.	44
Figure 3.17: Positioning system GUI module: A-motion parameter controls, B-motion displays, C-scanning parameters controls, D-motion controls.	45
Figure 3.18: DAQ module GUI.	47
Figure 3.19: The Welcome to Composer Application window.	48
Figure 3.20: ELMO Studio - coding environment.	49
Figure 4.1: Setup grounding.	52
Figure 4.2: Transfer Coefficient correction experiment.	55
Figure 4.3: Voice coil actuator response for different transfer coefficients (normalized).	56
Figure 4.4: CPD probe and distance sensor mounting.	57
Figure 4.5: Wafer Sample with Au and Ti films. Film width: A -500 micron, B-300 micron, C-100 micron.	58
Figure 4.6: Setting the reference point for the distance sensor (spindle is static) or scanning a track (spindle rotates).	60
Figure 4.7: Scanning routine.	62
Figure 5.1: Sample Profile: a) 3D Map, b) one track profile.	65
Figure 5.2: Profile data processing: track data without peaks and fitted curve.	65

Figure 5.3: a) Track profile and fitted curve, b) filtered profile surface.	67
Figure 5.4: Incline of the sample.	68
Figure 5.5: Wafer images taken using the classical nvCPD technique: 3D maps.	69
Figure 5.6: Track profile data.	69
Figure 5.7: Wafer images taken using the dynamic nvCPD system.	70
Figure 5.8: Track profile data.	71
Figure 5.9: Wafer images taken using both techniques: a) static nvCPD probe technique, b) terrain following technique.	72
Figure 5.10: Inner radius track.	73
Figure 5.11: Inner radius signals fragment with peaks.	74
Figure 5.12: Outer radius track.	75
Figure 5.13: Outer radius signals fragment with peaks.	76
Figure 5.14: Theoretical results for a) inner radius track, b) outer radius track.	77
Figure 5.15: CPD Probe area and fly height correlation.	79
Figure A.1: Closed Loop VCA operating diagram.	84
Figure A.2. Wire Diagram of the position system module.	88
Figure A.3: Wire Diagram of the position system module.	89

LIST OF SYMBOLS AND ABBREVIATIONS

Φ	Work Function
E_v	Vacuum Level Energy
E_f	Fermi Energy
V_{cpd}	Contact Potential Difference
e	Charge of an electron
Q	Electrical charge
C	Capacitance
ϵ_0	Permittivity of free space (8.8542×10^{-12})
ϵ_r	Relative permittivity/dielectric constant
A	Capacitor plate area/ Probe tip area
A_{ff}	Effective probe tip area/fringe field area
h	Plate separation distance/probe fly height
V_b	Voltage Bias
ω	Vibration Frequency
t	Time
i	Electrical current
V	Electrical potential
v	Linear velocity
Φ_p	Probe tip work function
x	Axis along which the probe translates
R	Radius of ideal probe tip or Electrical resistance

R_{ff}	Effective probe tip radius
N_{st}	Number of motion steps
V_0	Distance sensor output voltage in initial position
V_{cur}	Distance sensor output in current position
$V_{control}$	Output voltage difference of the distance sensor, $V_{cur} - V_0$
K_{tr}	Transfer coefficient to convert $V_{control}$ to number of steps
R^2	Goodness of fit
α	Surface incline angle
CPD	Contact Potential Difference
nvCPD	non-vibrating Contact Potential Difference
DAQ	Data acquisition
FWHM	Full-Width Half-Maximum
VCA	Voice Coil Actuator

SUMMARY

There is a large number of measurement techniques that is used for a surface inspection and a characterization of different types of materials. One of these techniques is a contact potential difference (CPD) scanning technique. In this project a non-vibrating contact potential difference (nvCPD) method is utilized to measure a work function and a topographical structure of a sample surface. A sample is mounted on a spindle that rotates at high speed. A nvCPD sensor detects work-function variations during movement above the sample surface.

There are certain factors that create difficulties during the measurement process. A nonplanar sample surface, the spindle wobble and an incline of a mounted sample impede the safe (without impacting the surface) scanning at a close distance. The goal of this thesis was to implement a height sensor as a feedback device to dynamically control and adjust a CPD sensor flying height. Since a CPD signal is inversely proportional to the flying height, minimization of this height will enhance the signal magnitude, the signal-to-noise ratio and the resolution of measurements.

A voice coil was used as a dynamic platform for the CPD sensor that accepted height sensor output as an input signal and adjusted the fly height. Two scans using improved and common nvCPD techniques were applied with the same experimental conditions. Results show an improvement of signal-to-noise ratio and resolution. For the described experiment amplitude of the signal increased by 25-100% and width of signal decreased by 15-25% compared to results from the common nvCPD scanning technique.

CHAPTER 1

INTRODUCTION

This thesis addresses the improvement of the non-vibrating contact potential difference (nvCPD) scanning technique which requires a minimum and relatively uniform height of scanning. An optical height sensor was used to obtain a profile of the surface, and the profile data and a voice coil was used to adjust the gap dynamically between the probe and the surface for each scanned track. Measurement results are compared with an analytical model of nvCPD probe tip response which accounts for the effect of fringing fields.

Contact potential difference is the difference in surface potential that is created when two conductive materials with different values of work function were electrically connected. The non-vibrating contact potential difference (nvCPD) probe measures the variation in the work function and topography of a sample by translating the probe over a surface. The probe signal strength varies with spacing between the probe tip and the surface being scanned.

The nvCPD technique can create image of the surface over a large area. The nvCPD measurement technique was utilized in different areas such as a lubricant measurement on a hard drive [1], a roller bearing defects detection [2], wear detection [3], wafer inspection [4], etc.

A probe tip and surface of interest form a capacitor. And because of this the CPD signal can be affected by different factors. The electrical field for parallel-plate capacitor

is generally assumed to be ideal [5, 7]. In practice, between the probe tip and a surface there is a fringe field effect [7, 8]. This effect increases the effective area of the probe tip, affecting the probe response and the resolution of the measurement [6]. The other factor that affects CPD signal significantly is a flying height. There is inversely proportional dependence between CPD signal and flying height [9, 11]. A minimization of the height improves the resolution of measurements, the signal magnitude and as a result signal-to-noise ratio.

A common setup for nvCPD measurement is a spindle with a mounted sample that rotates at high speed [4]. The nvCPD sensor detects the differential of the work-function and profile variations during movement above the sample surface. A nonplanar sample surface, spindle wobble and an incline of a mounted sample prevent a constant fly height (without impacting the surface).

CHAPTER 2

BACKGROUND

Work Function

The work function, Φ , of a material is the minimum energy required to remove an electron from the bulk to a point outside the surface (or energy needed to move an electron from the Fermi energy level into the vacuum). The work function is a characteristic property of metal and Figure 2.1 illustrates the work function of a metal as the difference between the Fermi energy and the vacuum level [10].

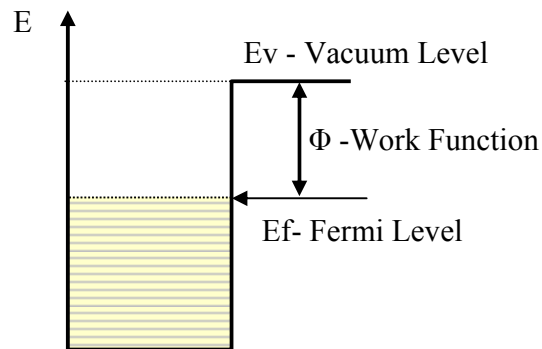


Figure 2.1: Schematic diagram of the work function and Fermi energy of a solid.

Since the electron has to move through the surface, its energy is affected by the mechanical, optical and electrical characteristics of the area. Thus, work function is extremely sensitive to surface conditions and is influenced by surface and bulk contamination, adsorbed or evaporated layers, surface charges, oxide layer imperfections, etc. All these surface conditions can be detected by measuring the work function. Many techniques have been developed based on different physical effects to measure the work function.

Contact Potential Difference

Contact potential difference is defined as the difference of electrical potentials developed between conductive materials under conditions of thermodynamic equilibrium. If two surfaces are brought in close proximity and are electrically connected then the Galvanic potential will drive electrons from one to the other until equilibrium is obtained. Electrons pass from the conductor with the lower work function to a conductor with the higher work function. As a result of this process conductors acquire electric charge of opposite signs (potential difference arises), which leads to the appearance of an electric field that prevents further electron transfer and Fermi levels equilibrium is reached [11]. Figure 2.2 shows the state of equilibrium between two metals of work functions Φ_1 and Φ_2 , before and after contact.

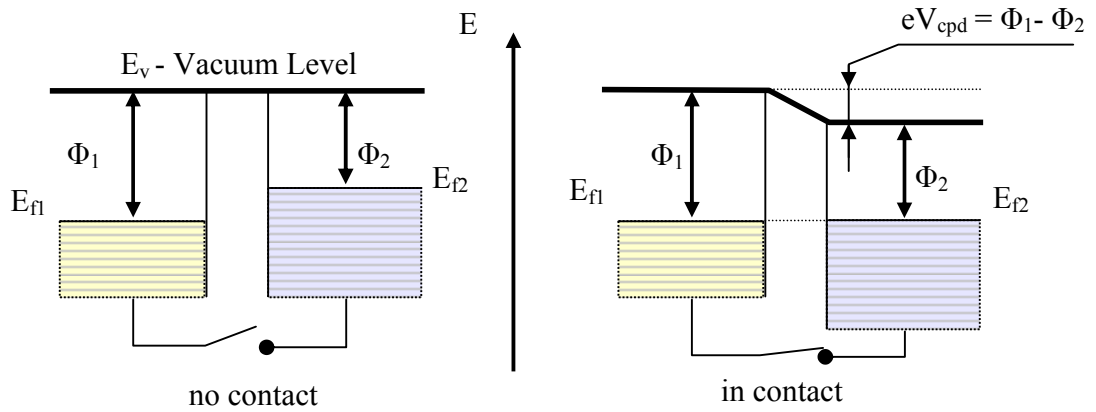


Figure 2.2: Schematic of contact potential difference.

The value of contact potential difference is equal to the difference between the work functions divided by electron charge

$$V_{cpd} = \frac{\Phi_1 - \Phi_2}{|e|} \quad (2.1)$$

Where

V_{cpd} is the contact potential difference,

$\Phi_{1,2}$ are the work functions,

$e = -1.6 \times 10^{-19} C$ is the electric charge carried by a single electron.

If the two surfaces of the materials are arranged into a parallel plate capacitor, the charge that flows between plates is proportional to the potential:

$$Q = CV_{cpd} \quad (2.2)$$

Where

Q is the charge on each plate,

C is the capacitance formed by the surfaces,

V_{cpd} is the contact potential difference.

For a parallel plate capacitor in which each surface separated by a uniform dielectric material, the capacitance C can be calculated as

$$C = \frac{\epsilon_0 \epsilon_r A}{h} \quad (2.3)$$

Where

$\epsilon_0 = 8.8542 \times 10^{-12}$ F/m is the permittivity of free space,

ϵ_r is the relative dielectric constant of the gap material between the plates,

A is the surface area common to both plates, and

h is the gap between the plates.

Equations (2.1), (2.2) and (2.3) represent the fundamental equations that are used in contact potential difference measurement to study characteristics of surfaces.

Kelvin Probe

The Kelvin Probe is a non-destructive, non-contact, vibrating device used to measure the work function difference between a conducting specimen and a vibrating tip. The Kelvin Probe is extremely sensitive to changes in the top atomic layers caused by adsorption, absorption, corrosion, atomic displacement, surface wear during sliding, oxidation, etc.

The Kelvin probe is named after Lord Kelvin. In 1898 Kelvin proposed an experiment to measure the contact potential difference using two flat polished discs of Zinc and Copper and a gold-leaf electroscope to measure the charge transfer upon

electrical contact [12]. The idea is to apply an external potential to the capacitor until the surface charges disappear, so the external potential equals the contact potential.

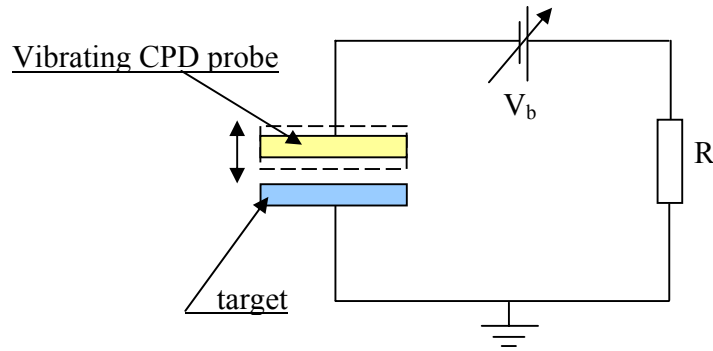


Figure 2.3: Schematic of Vibrating CPD probe

In 1932 William Zisman introduced a new method to measure the contact potential difference. He mounted a vibrating reference surface, or sensor, just above a sample electrode. The output voltage varied periodically as the tip vibrated, and the peak-to-peak voltage depended on the difference between the contact potential and external voltage [13]. A diagram of a typical vibrating Kelvin probe is shown in Figure 2.3. In the case of a vibrating probe tip, the distance between the plates h can be described as

$$h = h_0 + h_1 \sin(\omega t) \quad (2.4)$$

Where

h - the gap between the plates,

h_0 - the average distance between the plates,

h_1 - the amplitude of vibration,

ω - the frequency of vibration.

During vibration the capacitance of the system changes with respect to time:

$$C = \frac{\varepsilon_0 \varepsilon_r A}{h(t)} \quad (2.5)$$

The resultant current that flows between the surfaces is described by:

$$i = \frac{dQ}{dt} = \frac{d(CV_{cpd})}{dt} = V_{cpd} \frac{dC}{dt} + C \frac{dV_{cpd}}{dt} \quad (2.6)$$

Using Formula (2.5) and assuming that the contact potential difference for the given surfaces does not change ($\frac{dV_{cpd}}{dt} = 0$) (2.6) can be simplified:

$$i = V_{cpd} \frac{dC}{dt} = V_{cpd} \frac{d}{dt} \left(\frac{\varepsilon_0 \varepsilon_r A}{h_0 + h_1 \sin(\omega t)} \right) \quad (2.7)$$

The current $i(t)$ in the circuit can be nullified by applying a voltage bias V_b .

$$i = (V_b + V_{cpd}) \frac{d}{dt} \left(\frac{\varepsilon_0 \varepsilon_r A}{h_0 + h_1 \sin(\omega t)} \right) \quad (2.8)$$

When $i(t) = 0$ the voltage bias is equal to the contact potential difference for the pair of materials. If the work function for the tip is known the absolute value of work function for the other plate can be found using (2.1).

This method led to the development of systems that automatically track changes in the contact potential difference due to variation in the work function of samples.

Non-Vibrating CPD

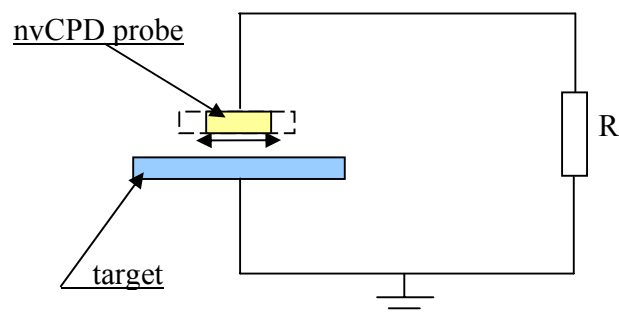


Figure 2.4: Schematic of Non-Vibrating CPD probe

An alternate method to perform CPD measurements by using translation was proposed by Danyluk and Zharin. Non-vibrating contact potential difference (nvCPD) technique uses translational motion between the probe tip and the surface of interest [3,14]. Relative motion of the tip results in electrical signals caused by geometrical or chemical changes on the opposite surface. Generated current is described by Equation 2.6. Each component of the equation represents topography and work function variations, Figure 2.5:

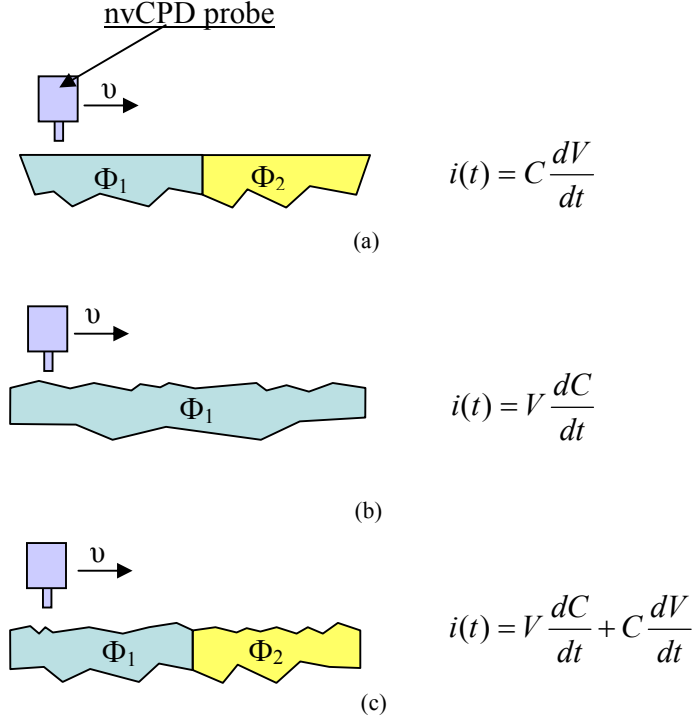


Figure 2.5: Schematic of the nvCPD probe passing over a surface:
(a) work function variation, (b) topography variation, (c) combination of (a) and (b).

nvCPD technique is commonly used for scanning a planar, smooth surfaces. In this case assuming a constant probe-to-target gap, the capacitance remains constant as the target is scanned, Figure 2.5(a). In this case, generated current can be expressed as

$$i(t) = C \frac{dV}{dt} \cong C \frac{\Delta V}{\Delta t} = C \frac{V_{cpd2} - V_{cpd1}}{\Delta t} \quad (2.8)$$

Where

V_{cpd1}, V_{cpd2} - the contact potential difference between the probe tip and the surfaces with work functions Φ_1, Φ_2 , respectively.

Consider Φ_p as the probe tip work function the contact potential differences will be

$$V_{cpd1} = \frac{\Phi_p - \Phi_1}{|e|} \quad (2.9)$$

$$V_{cpd2} = \frac{\Phi_p - \Phi_2}{|e|} \quad (2.10)$$

Inserting (2.9) and (2.10) into (2.8) yields

$$i(t) = \frac{C}{|e|} \frac{((\Phi_p - \Phi_2) - (\Phi_p - \Phi_1))}{\Delta t} = \frac{C}{|e|} \frac{(\Phi_1 - \Phi_2)}{\Delta t} \quad (2.11)$$

It follows from Equation 2.11 that the work function of the probe tip Φ_p does not contribute to the final signal and can not be used to calculate the absolute values of work functions. The signal reflects only relative changes in the contact potential difference of the surface in contrast to the Kelvin probe.

The main advantages of the nvCPD scanning technique are its simplicity and speed. The simple setup to utilize this technique is a stationary probe which scans rotating targets [4]. In practice, nvCPD probe tips are generally small for better spatial resolution and a gap between the probe tip and a target or “fly height” tends to be minimal for current conditions [15].

General form of the nvCPD response

An nvCPD probe is used to measure the change in work function as it translates over a feature. Figure 2.6 is a schematic of (a) a probe moving over a surface that contains an interface of work function Φ_1 and Φ_2 and (b) the expected signal versus spatial dimension.

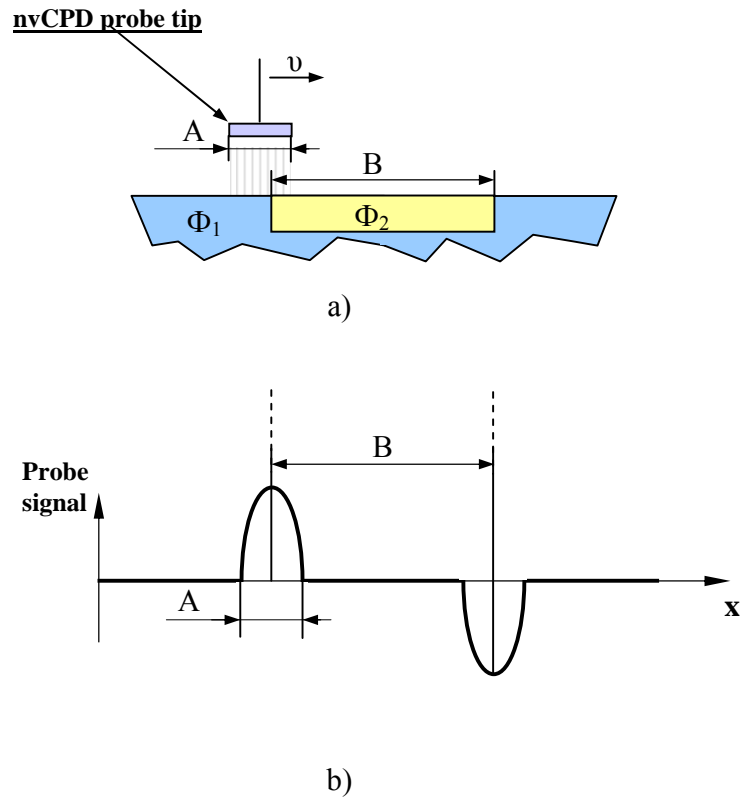


Figure 2.6: Schematic of a) the probe tip movement over a surface and b) expected nvCPD probe output for a given work function variation.

The figure shows a probe tip moving over a feature with a different work function. When the probe moves over a homogenous and planar surface at a fixed height, there will be no change in the CPD signal. As the probe approaches the interface the output signal will change due to the work function variation, $\frac{dV_{cpd}}{dt}$. When the probe leaves the boundary, the signal is zero again. This process repeats with an only change in a signal polarity when the probe is over the second interface. The polarity of the output peaks depends on the sign of $\frac{dV_{cpd}}{dt}$ ($\Phi_1 > \Phi_2$ or $\Phi_1 < \Phi_2$) [16]. In the ideal case, Figure 2.6, the width of the feature is equal to the peak-to-peak width of the nvCPD probe output, B, and the width of the probe tip can be estimated by measuring the width of a single peak A.

The analysis of the nvCPD probe response [17] starts with the output of the nvCPD probe as given by the equation:

$$i = V_{cpd} \frac{dC}{dt} + C \frac{dV_{cpd}}{dt} \quad (2.6)$$

where V_{cpd} is the contact potential difference and C is the capacitance between the probe tip and the surface of interest. It is assumed that surface and the probe tip are parallel and flat, and the topographical variation is negligible. Assuming that the signal only comes from the difference in work functions, i.e. there is no height variation and using Equation (2.3) for the capacitance, the nvCPD response simplifies to:

$$i = \frac{\epsilon_0 \epsilon_r A}{h} \frac{dV_{cpd}}{dt} \quad (2.12)$$

Expanding the work function variation term ($\frac{dV_{cpd}}{dt}$) yields:

$$i = \frac{\varepsilon_0 \varepsilon_r A}{h} \frac{dV_{cpd}}{dA} \frac{dA}{dt} \quad (2.13)$$

Where

$\frac{dV_{cpd}}{dA}$ is the contact potential difference change over a portion of the probe tip field area (dA),

$\frac{dA}{dt}$ is the change of that portion of the area with respect to time.

The last term can be expanded as:

$$i = \frac{\varepsilon_0 \varepsilon_r A}{h} \frac{dV_{cpd}}{dA} \frac{dA}{dx} \frac{dx}{dt} \quad (2.14)$$

Where

$\frac{dA}{dx}$ is the change of area with respect to axis \mathbf{x} , along which the probe moves.

Term $\frac{dx}{dt}$ is the relative velocity of the probe tip, ν , with respect to the surface of interest:

$$i = \frac{\varepsilon_0 \varepsilon_r A}{h} \frac{dV_{cpd}}{dA} \frac{dA}{dx} \nu \quad (2.15)$$

The derived Equation (2.15) presents the dependence of the nvCPD output on the input parameters (velocity, fly height, probe tip area). These parameters can vary during an experiment. The amplitude of the signal is proportional to the relative velocity of the probe tip with respect to the surface. For a rotating surface and a stationary probe, the nvCPD response is proportional to the rotation frequency. The amplitude of the signal is also proportional to the area of the probe tip, A , and inversely proportional to the fly height of the tip, h . These two parameters affect the resolution of measurements and signal-to-noise ratio.

nvCPD response of a round probe tip

For this research a round probe tip was used. Figure 2.7 shows a schematic of the round nvCPD probe tip moving over a flat surface with a feature on it with work functions Φ_1 and Φ_2 , respectively.

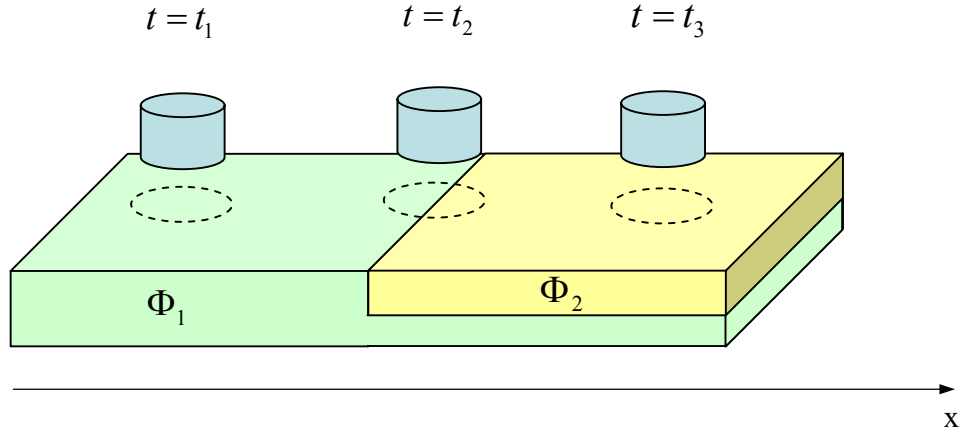


Figure 2.7: Schematic of round nvCPD probe tip translating over a surface with a feature.

These two regions result in a contact potential difference at the boundaries. This case is identical to the bimetal boundary translating example described in previous research on nvCPD probe response [17].

At times $t = t_1$ and $t = t_3$, $\frac{dV_{cpd}}{dA}$ and $\frac{dA}{dx}$ are zero because there is no work function variation over the homogeneous part of the surface. As a result, the nvCPD output is zero. At time $t = t_2$, the probe tip passes over the interface and the output

current is generated. In this case, $\frac{dV_{cpd}}{dA}$ is a step change in work function from Φ_1 to Φ_2 , at the feature boundary. The term $\frac{dA}{dx}$ is the change in area of the feature in relation to the whole probe field area, which is the same as the probe tip area, A , for the ideal case. As shown in Figure 2.7, at time $t = t_2$ the probe tip area consists of two areas of work functions Φ_1 and Φ_2 . It was proved that the change in area, $\frac{dA}{dx}$, is the change in the area of Φ_2 within the probe field, A [17]. The area of Φ_2 is A_I and can be calculated in terms of distance of the feature boundary, x , from the probe center by solving the geometrical problem, Figure 2.7.

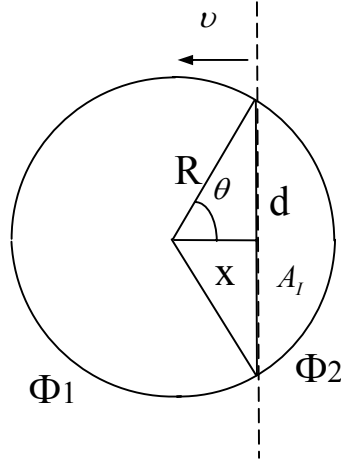


Figure 2.8: Geometry of nvCPD probe passing the boundary of the feature.

The area A_I can be calculated as the area difference of the sector and the triangle:

$$A_I = R^2\theta - xd \quad (2.16)$$

Where

R is the probe tip field radius,

θ is the angle shown in Figure 2.8, with a range of $0^\circ \leq \theta \leq 180^\circ$,

x is the distance, with a range of $-R \leq x \leq R$.

In terms of x it can be written:

$$A_I = R^2 \arccos\left(\frac{x}{R}\right) - x\sqrt{R^2 - x^2} \quad (2.17)$$

The change in area $\frac{dA}{dx}$ is found by differentiating Equation (2.17):

$$\frac{dA_I}{dx} = \frac{-R}{\sqrt{1 - \frac{x^2}{R^2}}} - \sqrt{R^2 - x^2} + \frac{x^2}{\sqrt{R^2 - x^2}} \quad (2.18)$$

which can be simplified to:

$$\frac{dA_I}{dx} = -2\sqrt{R^2 - x^2} \quad (2.19)$$

Substituting into Equation (2.15), a complete nvCPD response model for an ideal round probe tip is given by

$$i = \frac{\varepsilon_0 \varepsilon_r A \nu}{h} \frac{dV_{cpd}}{dA} (-2\sqrt{R^2 - x^2}) \quad (2.20)$$

where ε_r , A , h , and ν are experimental constants in this example. The value of

$\frac{dV_{cpd}}{dA}$ is a constant for stable surfaces. The last term of Equation (2.20) in parentheses

describes the shape of the output signal and valid only for the range $|x| \leq R$. It is a semicircle with a radius R .

The described model allows a prediction and estimate of the relative change of nvCPD response with respect to fly height and a comparison with the measurement. Even though the ideal probe tip was considered for this model it can be modified to account for real-life factors. Note that the effective radius and the area of the field beneath the probe are affected by the fringe field and depends on the fly height [9, 17]. The presence of the radius term in the model allows for estimating the influence of the fly height variation on the measurement resolution.

Effect of Fringe Fields on nvCPD Response Model

The ideal nvCPD probe tip response discussed before assumes that a homogeneous electrical field between the surface and the probe is equal in shape and size to the probe tip [5,7,18]. These assumptions are used in the capacitance calculation given in Equation 2.3 and shown in Figure 2.9(a).

$$C = \frac{\epsilon_0 \epsilon_r A}{h} \quad (2.3)$$

In practice, when the distance between the capacitor plates is comparable with plate areas the edge effect of a capacitor can not be neglected [9,19], Figure 2.9(b).

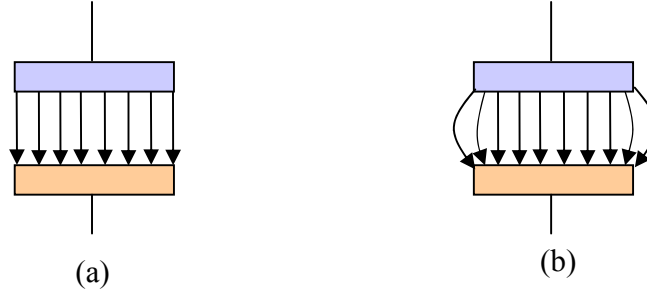


Figure 2.9: Schematic of the electrical fields for an ideal (a) and a real (b) capacitor

Fringe fields are important for the scanning applications because they change the effective area of the probe tip affecting lateral resolution and sensitivity of the probe.

In the previous section it was shown that the shape of the nvCPD output signal depends on the shape of the probe, Equation (2.20). As shown in Figure 2.10(a), the width of the signal from an ideal probe tip is equal to the probe tip width. Figure 2.10(b) shows that for a real probe tip, the width of the output signal is wider and can be estimated by the field width at the surface of interest.

The response model described above, Equation (2.20), can be changed to consider the influence of the fringe field. If the field is assumed to be round, then Equation (2.20) can be rewritten:

$$i = \frac{\varepsilon_0 \varepsilon_r A_{ff} \nu}{h} \frac{dV_{cpd}}{dA} (-2\sqrt{R_{ff}^2 - x^2}) \quad (2.21)$$

where the probe tip radius R and the area A has been replaced with the fringe field radius R_{ff} and the area A_{ff} .

For the ideal conditions when the fringe fields are neglected and the only variable is fly height the nvCPD output dependence is defined as :

$$i \sim \frac{1}{h} \quad (2.22)$$

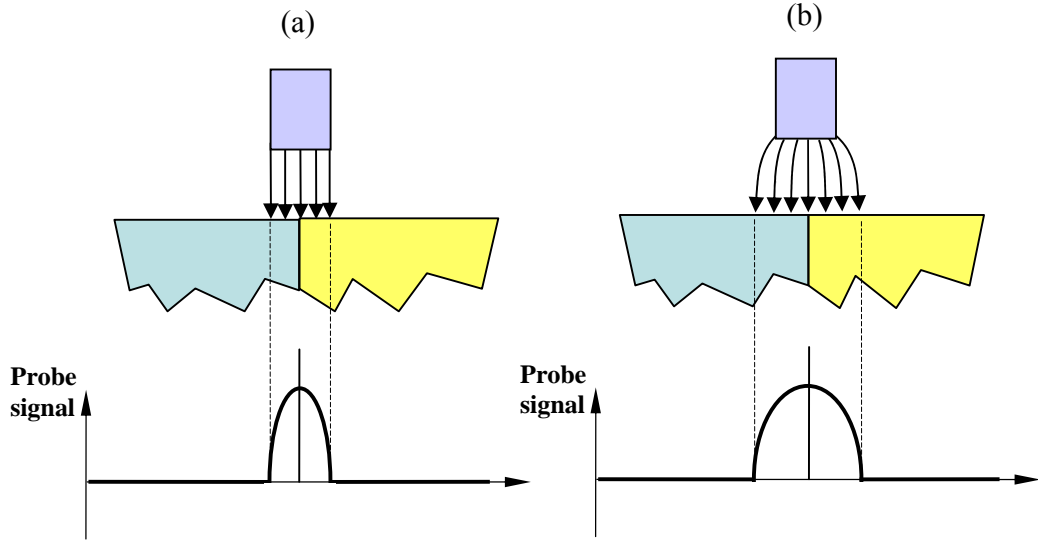


Figure 2.10: Schematic of the nvCPD response for an ideal (a) and a real (b) case.

When the fringe field is included in the analysis, the area A_{ff} and the radius R_{ff} (for a round probe) are functions of the fly height h . In this case, the shape of the output signal changes with respect to fly height and the magnitude of the output depends on h as:

$$i \sim \frac{A_{ff}(h)}{h} \quad (2.23)$$

where A_{ff} is the effective area of the probe tip considering the fringe field.

From Equation 2.23 it is important to note that the probe tip output is influenced by the fly height directly and indirectly through the fringe fields. The fringe field affects nvCPD spatial resolution by increasing the effective area of the probe tip. By minimizing

the fly height the magnitude of nvCPD output will be enhanced and the effective area of the field will converge to the actual area of the probe tip.

The modified nvCPD probe response can be used to estimate relative improvement of the signal magnitude and lateral resolution if the functional dependence between the effective radius and fly height is known.

A wide variety of formulas were derived by fringe field researchers to reflect the fringe field effect on the parallel plate capacitor, but most of the results provide the true capacitance equations (with fringe field effect), or a correction to the capacitance calculated without fringe field effect [8,19,20,21]. They do not reflect the dependence of effective radius or area on a gap or fly height.

An uncomplicated fringe field formula that bound the gap and effective geometry of the capacitor is given by Mackel in the Kelvin microscope analysis [22]. A quarter of the probe fly height, h , is added to the radius of the probe tip and the field is treated as homogeneous. In mathematical form, this linear approximation is:

$$R_{ff} = R + \frac{1}{4}h \quad (2.24)$$

Substituting into Equation 2.21, the nvCPD response can be rewritten as:

$$i = \frac{\varepsilon_0 \varepsilon_r \pi (R + \frac{1}{4}h)^2 \nu}{h} \frac{dV_{cpd}}{dA} (-2\sqrt{(R + \frac{1}{4}h)^2 - x^2}) \quad (2.25)$$

Typical nvCPD scanning setup and difficulties

As mentioned previously, the non-vibrating CPD sensor is used for fast scanning and visualization of contact potential topology on material surfaces. The nvCPD scanning technique has been used in different applications such as analysis of lubricants on magnetic media [1,23], surface characterization of hard disks[24], semiconductor wafer inspection system [4].

Typical nvCPD scanning system includes an X-Y-Z positioning system, a rotating stage, a high speed data acquisition system, a PC and control software. The surface of interest is fixed to a rotating spindle. The nvCPD sensor is positioned at a fixed distance from the surface on a positioning system, Figure 2.11. The specimen is then rotated at a high speed, and the nvCPD sensor is translated radially to collect data in circumferential tracks. The tracks of data are then put together to compare a CPD image. These CPD images visualize chemical and geometrical defects and features of the surface.

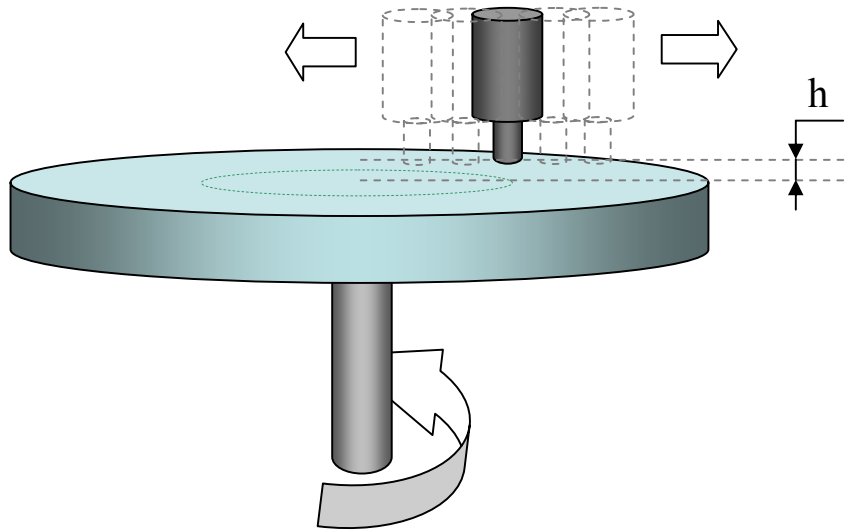


Figure 2.11: Typical nvCPD scanning system.

There is one distinguishing feature of this technique. The scanning process is performed with constant fly height defined at the very beginning of the scanning process. As discussed previously, this parameter is critical for the signal-to-noise ratio and resolution. Thus, to achieve the best results of scanning the CPD sensor has to be positioned as close as possible to the surface of interest. However there are certain factors that create difficulties during the scanning procedure, Figure 2.12.

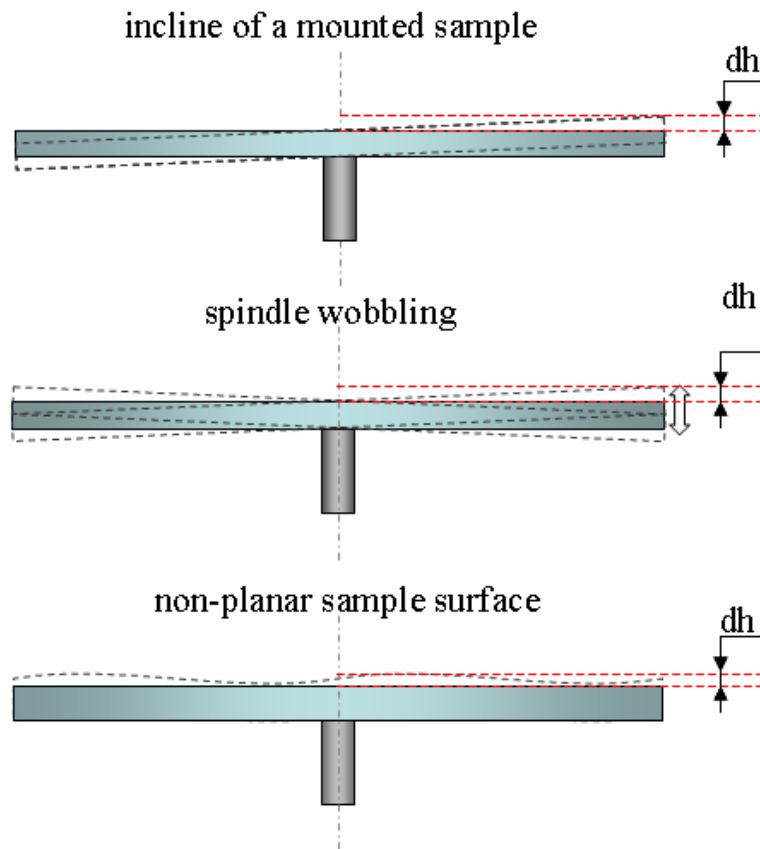


Figure 2.12: Difficulties during the measurement process: incline, wobbling, non-planar surface.

A non-planar sample surface, a spindle wobbling and an incline of a mounted sample impede safe scanning at a close and uniform distance. Thus, it can be seen that there is a need for an improvement for the scanning technique by providing means and a procedure for dynamic adjustment of the fly height during the scanning. The main idea of the scanning improvement is presented in the Figure 2.13:

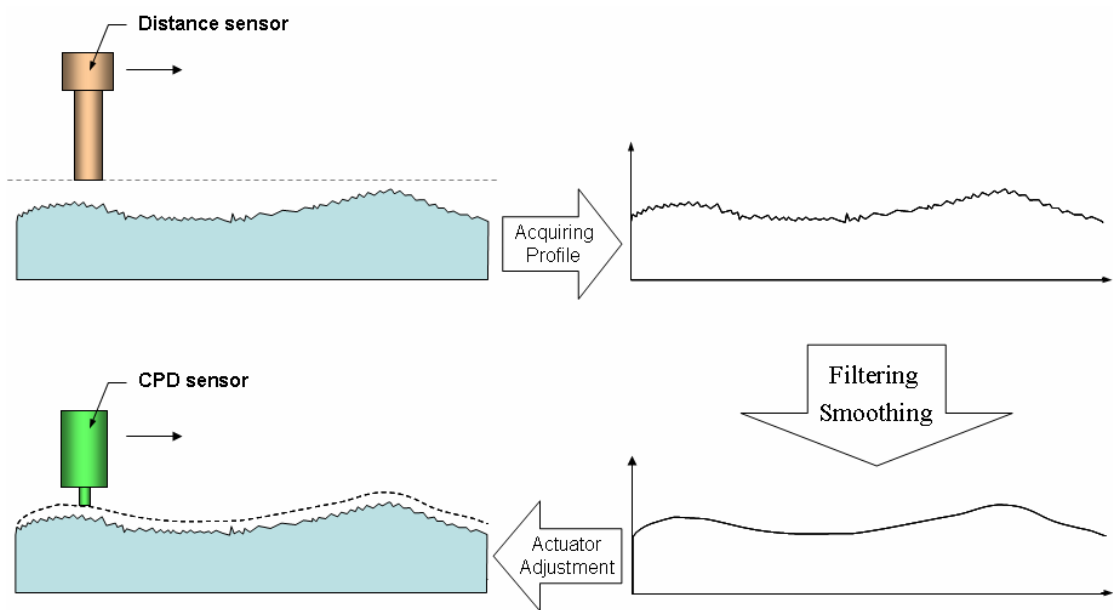


Figure 2.13: Modified nvCPD Scanning technique.

Before acquiring CPD data from the track, a distance sensor is used to determine a profile of the track. Then this signal is processed, filtered and, smoothed. Afterwards the signal is used as a control signal to adjust a voice coil with a CPD sensor mounted on it to follow the surface at a relatively uniform height.

Experimental Plan

The flowchart displayed in Figure 2.14 shows the research plan carried out in order to improve nvCPD scanning technique. All the steps in the flowchart are explained in detail in different parts of this thesis.

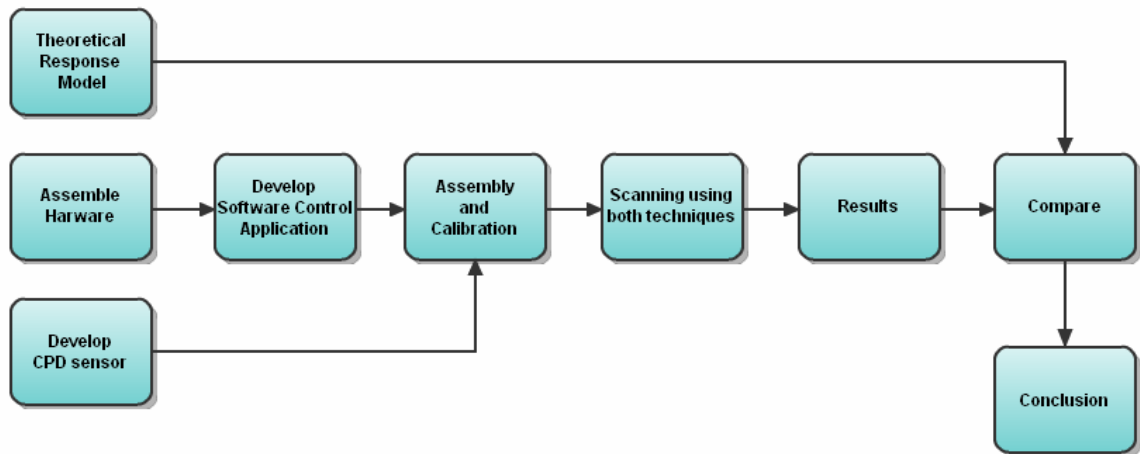


Figure 2.14: Experimental Plan.

CHAPTER 3

EXPERIMENTAL DETAILS

The experimental setup included commercially available test equipment as well as custom designed components. Most of these components were controlled by a host computer using software written in LabView. In this chapter the experimental details are described.

Overall System Architecture

The experimental setup consisted of six subsystems: a positioning system, a CPD sensor, a waveform generator, a voice coil actuator, distance sensor and a data acquisition system. A photograph of the setup is shown in Figure 3.1, and a simplified diagram of the main components is shown in Figure 3.2.

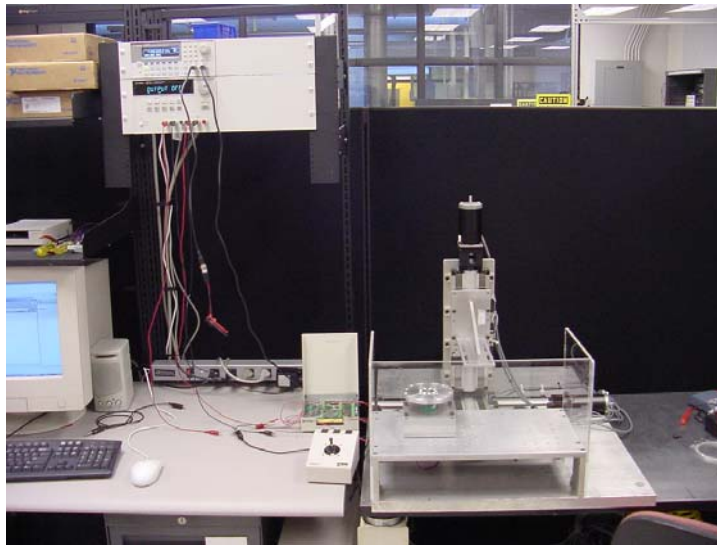


Figure 3.1: Photograph of Experimental Setup.

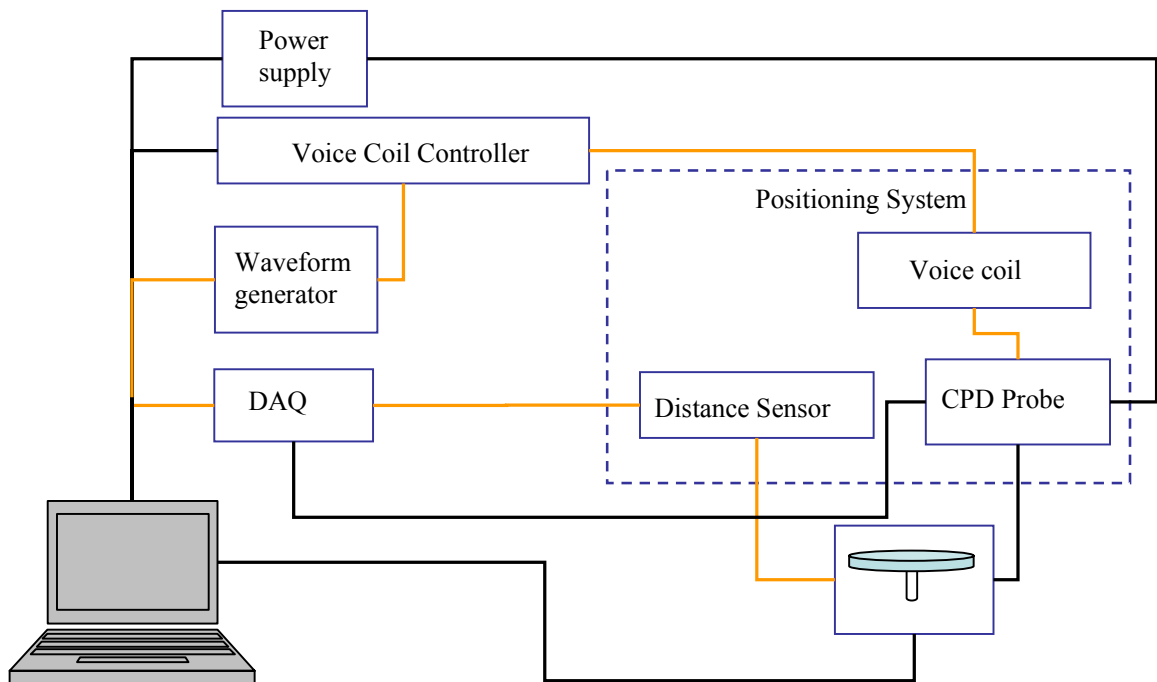


Figure 3.2: Schematic diagram of the system.

The following sections include details and specifications for the hardware and software components of the system.

Hardware

Positioning System

The XYZ motion of the CPD probe included a positioning system that consisted of the following components:

- Three “S57-102MO” stepper motors
- Three “Daedal XR404 Series” linear motion tables
- Three microstepping drives “ZETA4”
- One AT6400 indexer
- One AT6400 PC ISA card

X and Y axes tables had 250mm of travel and Z-axis table had 100 mm of travel. Position repeatability was 1.3 microns, and positional accuracy was 8 microns, backlash was less than 0.200°. The linear tables were mounted on a test platform, Figure 3.3. X-axis table carried Y and Z tables along the x axis. The Y-axis table in turn carried the Z-axis along the y axis. Finally the Z table carried the CPD probe and the other hardware along the z axis. Thus, the system provided 3D motion for the hardware mounted on the Z-table.

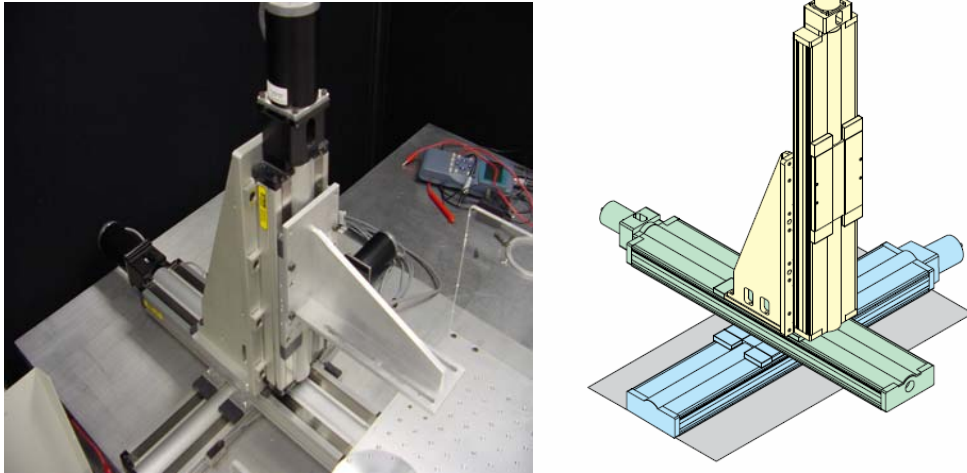


Figure 3.3: XYZ-positioning system

The stepper motors were physically mounted on the positioning tables and were used to drive the tables. The motors were controlled by the microstepping drives. The accuracy and repeatability of these modules are 0.0833° and 0.0014° correspondingly. The resolution was 50 800 steps per revolution, which gave a linear resolution of 0.4 microns for the 20mm ballscrew. Steps and directions of the motor rotations were defined by the “AT6400” indexer signals. A schematic diagram of system components is shown in Figure 3.4.

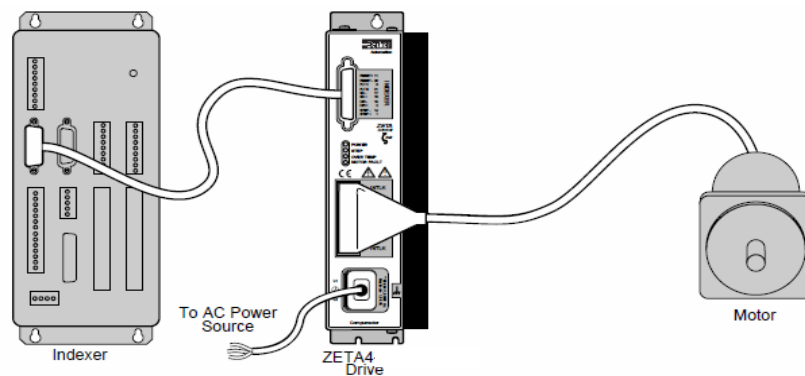


Figure 3.4: Schematic diagram of position system components.

The positioning system was manipulated by sending commands from a host computer. The AT6400 PC card was installed in the computer to provide a connection to the system components. The card converted the high-level commands to the instructions, understandable for the indexer. Step pulses were generated in the indexer and sent to the drives with a rate up to 1.6MHz. Finally, the analog current from the drives produced motion on the step per motors, Figure 3.5.

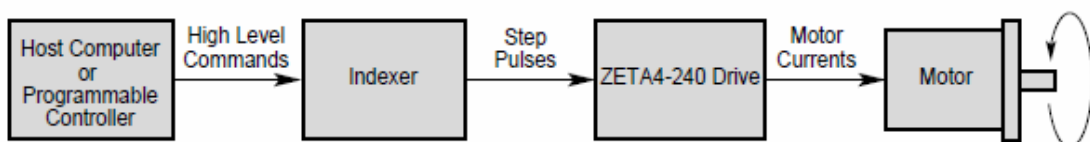


Figure 3.5: Block diagram of position system.

The system delay was negligible (in order of 10^{-6} s) thus the system was controlled in real time.

Optical distance sensor

A “MTI-2000 Fotonic” fiber optic system was used as a distance sensor to measure a vibration and a profile of a surface of interest.

The fiber optic sensor transmits a beam of light through a flexible fiber-optic probe, receives reflected light from a surface, and converts this light into an electrical signal. The output signal voltage is proportional to the distance between the probe tip and the surface and is used to determine displacement, vibration amplitude, and profile of a target surface [25]. A fiber optic concept is shown in Figure 3.6.

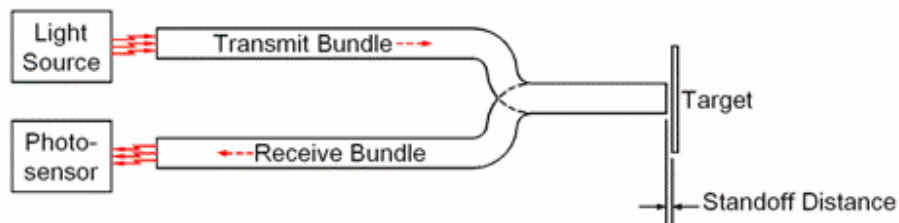


Figure 3.6: Fiber Optic Probe Principle.

Figure 3.7 shows that when a fiber optic probe is close to a target, the receiving fibers (B) can see only the small amount of reflected light (A). This is due to the fact that the fiber can propagate light that enters the fiber within a certain cone, called the acceptance cone. These cones are shown in the figure and overlapped area represents the amount of light reflected and received by the fibers B [26]. Thus, even small surface movements farther away from the probe cause a significant increase in the amount of received light, Figure 3.8.

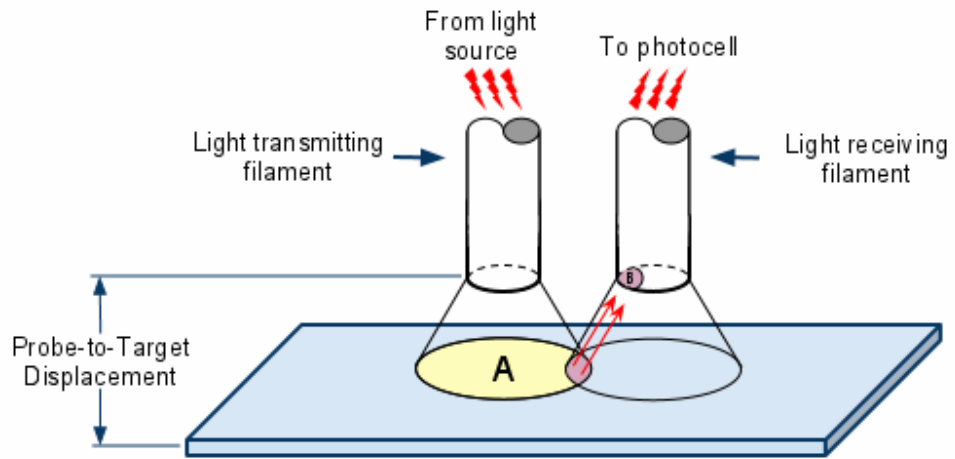


Figure 3.7: Sensor reflected light, close to target.

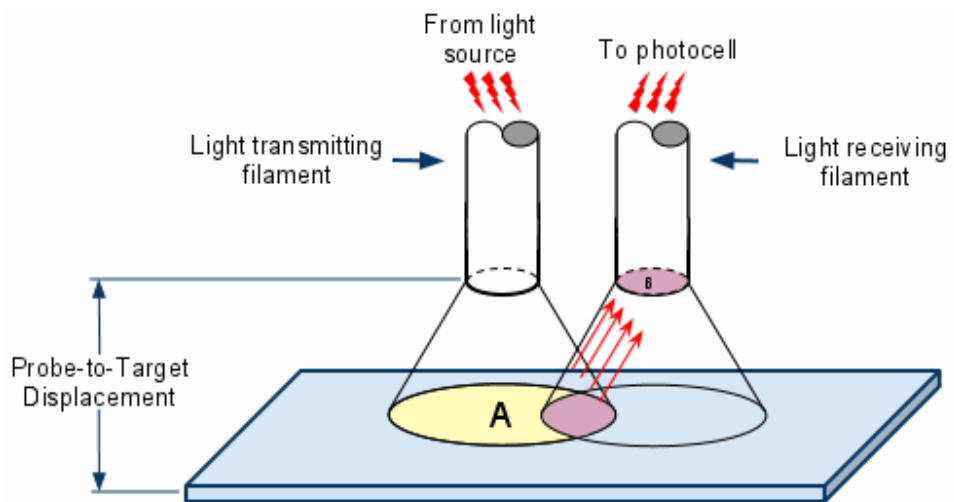


Figure 3.8: Maximum reflected light from Fiber Optic Sensor.

Further increasing of the “target-probe” distance causes saturation of the receiving fiber due to enlargement of the area A. At this point the sensor generates the maximal output signal. Further surface movement away from the probe causes a decrease in the output signal in consequence of the light intensity loss, Figure 3.9.

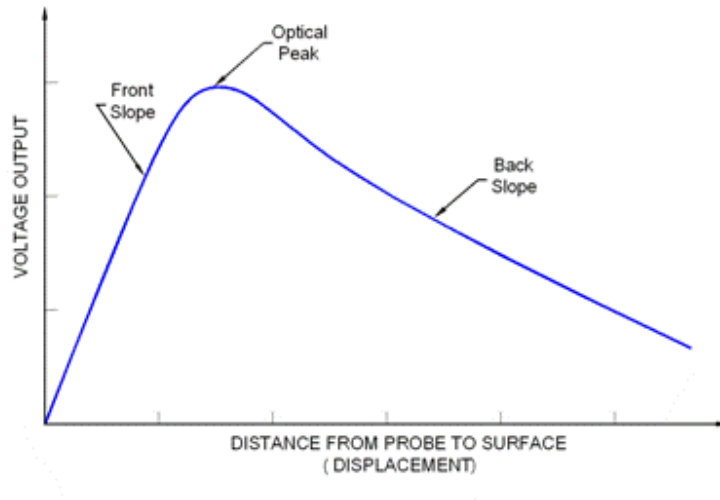


Figure 3.9: Typical Fiber Optic Probe response curve.

Thus, each probe had two operating ranges, one (front slope) for high resolution with a small standoff and the other (back slope) less sensitive with a larger standoff and measurement range. This allowed using the same probe in different experimental conditions.

The MTI-2000 has a modular design that allowed using interchangeable fiber-optic probe modules. In this research two probe modules with different specifications were used: MTI2032R and MTI2125H. The probes were mounted on the Z-axis table of the positioning system. Measurement characteristics for the modules are given in Table 3.1. The table specifies values for the geometric size of the sensors, frequency response, resolution and sensitivity for each range on the response curve described before. The sensitivity values were used to calculate transfer coefficient to convert output voltage from the height sensor to the voice coil steps. The calculations are described in the next chapter. Each probe module has integral high and low-pass filters that increased the resolution of the measurement. The high resolution and sensitivity of the modules were

sufficient for the needs of this project. For example, the resolution and sensitivity for the module MTI2125H used as a main height sensor were 0.25 and 0.33 microns correspondingly. Because these values beyond the resolution of the height actuator (micron range) did not limit the performance of the system. The dual-channel capability of the system, that makes simultaneous measurements with two probe modules possible, was used to calibrate and calculate the calibration and feedback parameters for the voice coil control system.

Table 3.1: Measurements specification for fiber optic probe modules.

Probe Module Model Number		MTI2032R	MTI2125H
Probe Tip Diameter in. (mm)	Total	0.032 (0.813)	0.125 (3.175)
	Active	0.019 (0.483)	0.090 (2.286)
Maximum Frequency Response (-3dB) kHz		130	150
Output Signal Noise mV p-p		20	3
Meter Resolution μ in. (μ m)	Range 1	1.0 (0.03)	10.0 (0.25)
	Range 2	10.0 (0.25)	10.0 (0.25)
Range1 Characteristics	Sensitivity $\frac{\mu\text{in}}{\text{mV}} (\frac{\mu\text{m}}{\text{mV}})$	0.74 (0.02)	13.0 (0.33)
	Linear Range mils (mm)	5.0 (0.13)	80 (2.03)
	Standoff mils (mm)	3.0 (0.17)	130 (3.30)
Range2 Characteristics	Sensitivity $\frac{\mu\text{in}}{\text{mV}} (\frac{\mu\text{m}}{\text{mV}})$	4.1 (0.1)	45.0 (1.14)
	Linear Range mils (mm)	29.0 (0.74)	208.0 (5.28)
	Standoff mils (mm)	30.0 (0.76)	350.0 (8.89)
Optical Peak mils (mm)	Midpoint	15.0 (0.38)	240.0 (6.10)
	Range	10.0 (0.25)	44.0 (1.12)

Data Acquisition

The data acquisition hardware system consisted of a National Instruments (NI) PCI-6251 data acquisition card (DAQ) connected to a NI SCB-68 connector block. The SCB block analog inputs were connected directly to the CPD probe output. The DAQ was inserted in a PCI slot in the host computer and used to digitize an analog CPD signal with certain parameters. The DAQ features were [27]:

- 16 inputs at 16 bits, 1.25 MS/s
- 2 analog outputs at 16 bits, 2.8 MS/s
- 7 programmable input ranges (± 100 mV to ± 10 V) per channel
- Analog and digital triggering.

Waveform Generator

An Agilent 33220A waveform generator was used to provide an arbitrary waveform during the scanning procedure. The Agilent 33220A was selected for its frequency stability (range: 1 μ Hz to 20MHz), low distortion (-35..-75dBc), ability to generate 14 bit 64k-point arbitrary waveform with sample rate 50MSa/s and ease of use due to its programming capability through USB and GPIB connection, Figure 3.10.



Figure 3.10: Waveform generator Agilent 33220A.

During any single experiment, profile data were recorded using the fiber optic sensor and were sent to the function generator through a USB interface to reproduce the same waveform. This generated signal was used to control the motion of a voice coil actuator and the CPD sensor mounted on it. Common and arbitrary waveform characteristics are presented in Table 3.2 [28].

It has to be noted that sample rate of 50MSa/s for the arbitrary waveform was more than enough for the purpose of the experiments since the sample rate for the target signal was up to 100 kHz. The waveform length of 64k points complied with the requirements as well since each track profile contained up to 10k points. The amplitude resolution of 14 bit allowed accuracy of 1mV for the reproduced signal that corresponded to the submicron distance region.

Table 3.2: Common and arbitrary waveform characteristics Agilent 33220A.

Common Characteristics		
Frequency	Accuracy	$\pm (10 \text{ ppm} + 3 \text{ pHz})$ in 90 days $\pm (20 \text{ ppm} + 3 \text{ pHz})$ in 1 year
	Resolution	1 μHz
Amplitude	Range	10 mVpp to 10 Vpp into 50 Ω 20 mVpp to 20 Vpp into open circuit
	Accuracy	$\pm 1\%$ of setting $\pm 1 \text{ mVpp}$
	Units	Vpp, Vrms, dBm
	Resolution	4 digits
DC Offset	Range	$\pm 5 \text{ V}$ into 50 Ω $\pm 10 \text{ V}$ into open circuit
	Accuracy	$\pm 2\%$ of offset setting $\pm 0.5\%$ of amplitude $\pm 2 \text{ mV}$
	Resolution	4 digits
Arbitrary waveform		
Frequency range	1 μHz to 6 MHz	
Waveform length	2 to 64 k points	
Amplitude resolution	14 bits (including sign)	
Sample rate	50 MSa/s	
Min. Rise/Fall Time	35 ns typical	
Linearity	$< 0.1\%$ of peak output	
Settling Time	$< 250 \text{ ns}$ to 0.5% of final value	
Jitter (RMS)	6 ns + 30 ppm	

Voice Coil Actuator

A Voice Coil Actuator (VCA) NCM02-17-035-2FE01 from H2W Technologies was chosen to control the CPD probe motion along the Z-axis during scanning. The actuator was contained in a steel housing, which constrained the magnetic field through the coil, Figure 3.11. VCM was mounted on Z-axis table of the positioning system and served as a mobile platform for the CPD sensor.

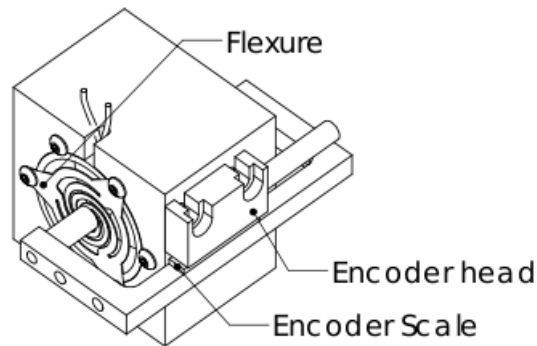


Figure 3.11: Voice Coil Actuator NCM02-17-035-2FE01.

The VCA is a direct drive motor that employs a permanent magnetic field and coil winding to produce a force proportional to the current applied to the coil. These motors have no hysteresis and therefore have a linear current-vs-position dependence. The stroke or displacement for this model was $\pm 2.8\text{mm}$, continuous force 16N and the encoder resolution was 5 microns . To provide high accuracy and repeatability the VCA operated in a closed loop [29], Figure 3.12. This required a linear encoder, linear amplifier, and programmable motion controller.

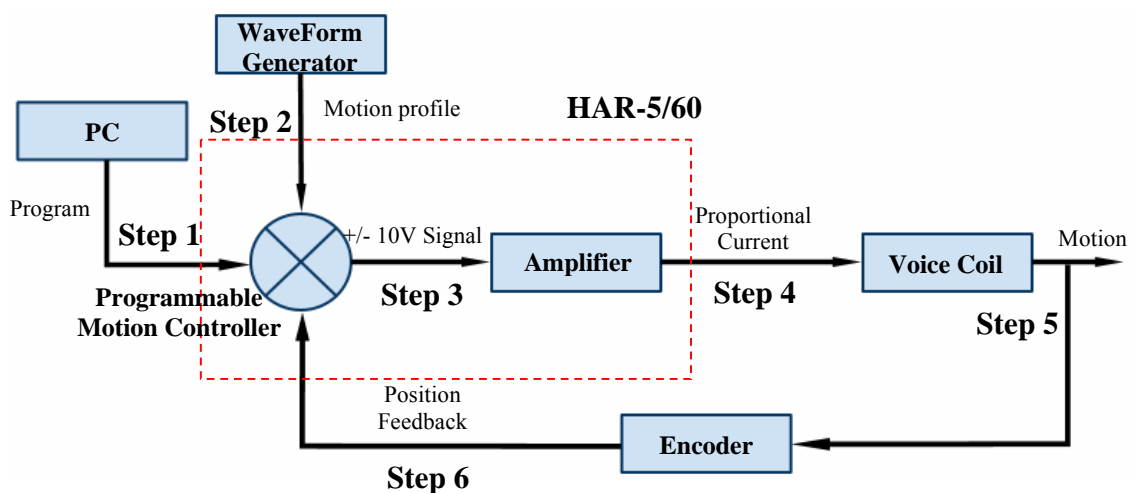


Figure 3.12: Closed Loop VCA operating diagram.

An Elmo HAR -5/60-1 drive was used as a programmable motion controller and an amplifier, Figure 3.13a. A Magnetic Band MB500, Magnetic Sensor MS500 and AS510/1 translation module were used as a position feedback system, Figure 3.13b. Detailed information on the specifications of the HAR -5/60 and AS510/1 is presented in Appendix A as well as a step-by -step description of the Closed Loop operating diagram.



Figure 3.13: a) Elmo HAR -5/60-1 drive; b) AS510 translation module.

CPD Probe Circuit

The CPD sensor circuit described below and used in this project was built using Dr. Anatoly Zharin's design. A schematic diagram of the circuit is shown in Figure 3.14.

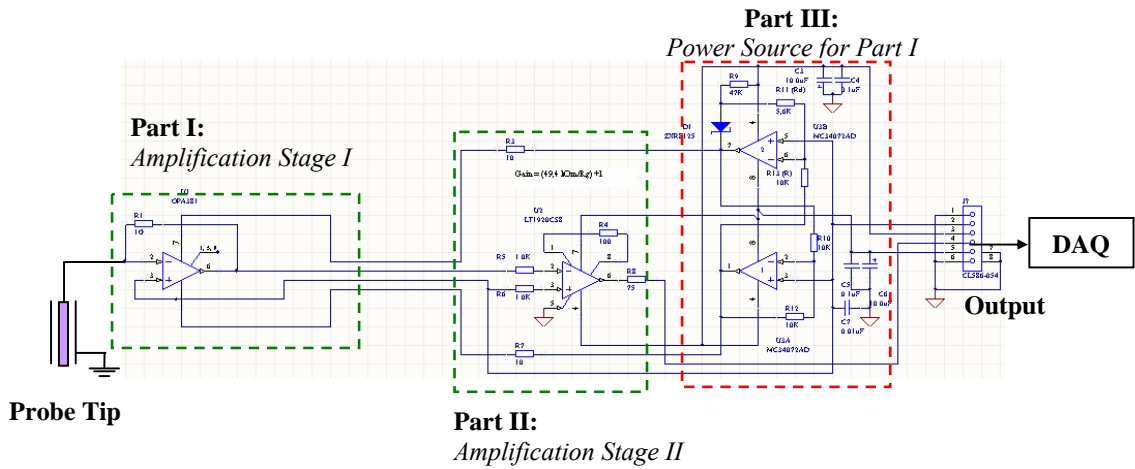


Figure 3.14: Circuit diagram of CPD sensor.

Since the signal generated in the CPD probe is a very weak current, the circuit was designed to convert the current into a voltage and amplify it. The circuit could be divided in three parts. The first two parts were amplification stages and the last part was a power source for the first amplification stage.

The first part had a high-speed precision operational amplifier and high-ohmic feedback resistor. The second part consisted of a single-resistor gain-programmable precision instrumentation amplifier. For the first stage transimpedance amplifier an OPA381 was used. This amplifier provided high precision, long-term stability and low noise. For the second stage, the LT1920CS8 precision instrumentation amplifier was used. This amplifier required only one external resistor to set the gain. The circuit was driven by a $\pm 12V$ power source. All components used for the circuit are given in Table 3.3.

Table 3.3: Components of the CPD sensor circuit.

R1=1G Ω R3,R7=10 Ω	C3, C6=10 μ F	DZXRE125
R4,R11=5.6k Ω	C4,C5=0.1 μ F	OPA381
R5,R6=1 k Ω	C7=0.01 μ F	LT1920CS8
R8=75 Ω		MC34072AD
R9=4 k Ω		MC34072AD
R10,R12, R13=10 k Ω		

A photograph of the CPD sensor electronics is shown in Figure 3.15.

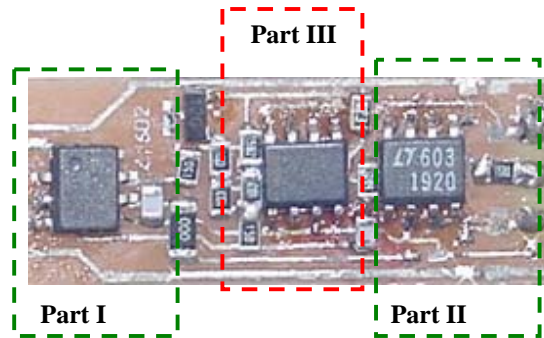


Figure 3.15: CPD sensor photograph.

Software

Several software applications were written and used to operate the hardware described in the previous section. This section is a description of the software used in the research.

A software application that controlled the positioning system, the waveform generator, the power supply and the data acquisition from the CPD sensor was written in a graphical programming environment LabView (from National Instruments). The Labview environment was chosen because of the ease of use in user graphic interface designing and the availability of all necessary libraries and drivers for the Labview from the hardware manufacturer. The Labview provided hundreds of built-in libraries for advanced analysis and data visualization as well. The written application communicated with the DAQ PC card and the indexer ISA card installed in the PC to control incoming data from the CPD sensor and its motion over a sample surface. A graphic user interface was also provided to control hardware, to visualize and monitor signals and to set up measurement parameters as well. The application was used to postprocess data and visualize results of surface scanning in 2D and 3D view. A schematic diagram of the application is displayed in Figure 3.16.

Positioning system software

The positioning system manufacturer provided the software routine libraries to help to develop programs for the 6400 series motion controller. These libraries were compiled in the Labview to make it usable in this environment.

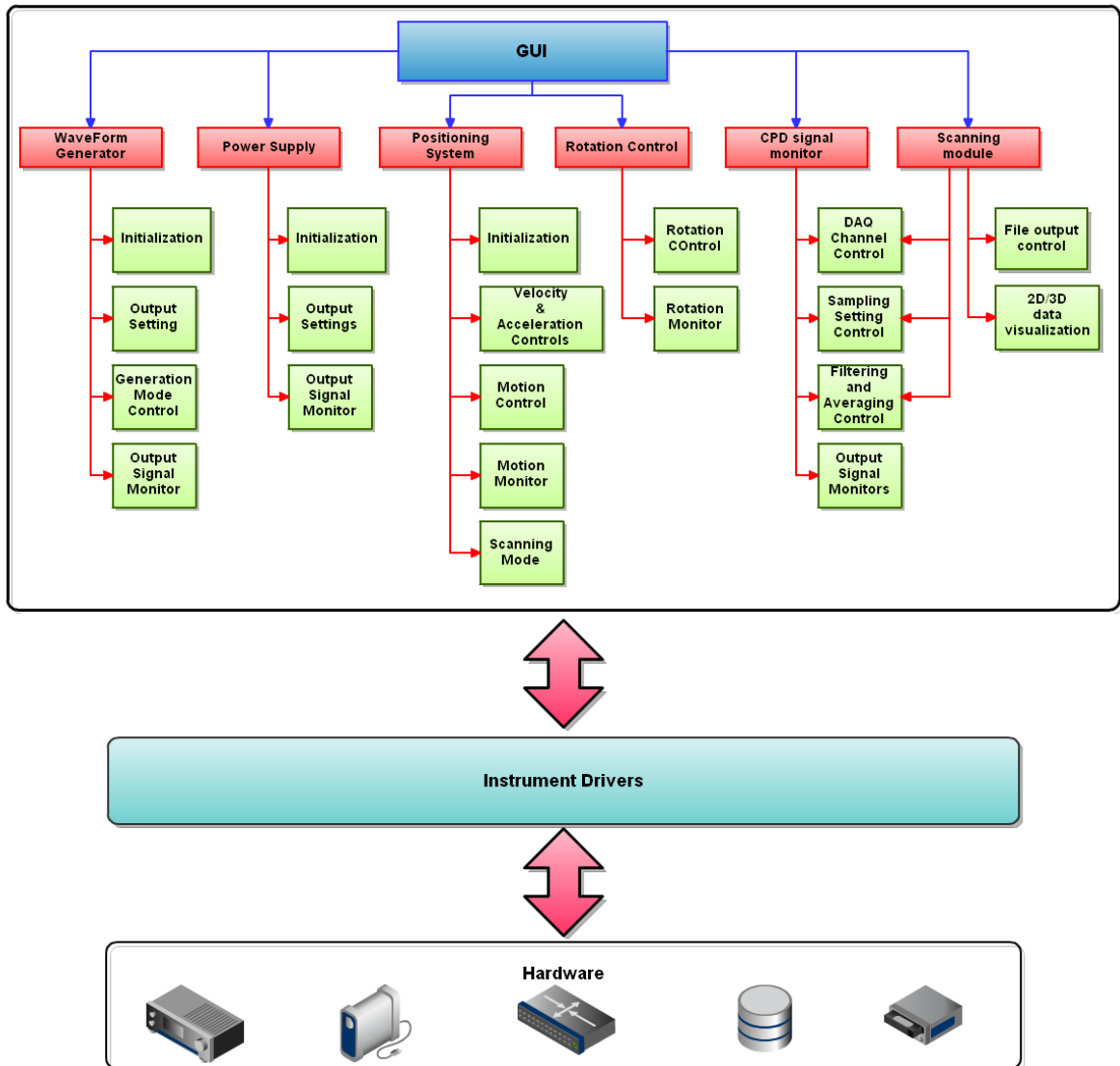


Figure 3.16: Schematic diagram of the Labview application.

Using routines from compiled libraries the application communicated through the PC ISA card with the indexer to control velocity, direction and acceleration of the motion of the CPD sensor. The front panel of the positioning system module was designed to

make it suitable for intuitive motion control and visualization. The picture of this module is shown in Figure 3.17.

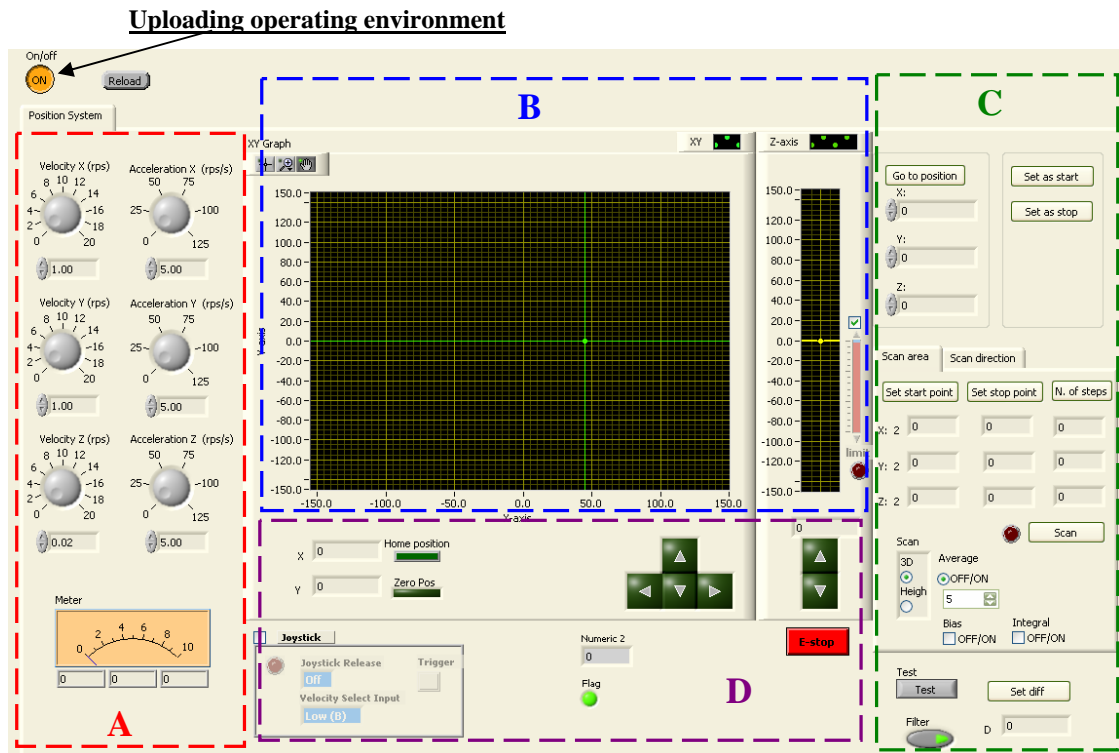


Figure 3.17: Positioning system GUI module: A-motion parameter controls, B- motion displays, C- scanning parameters controls, D- motion controls.

After activation of the module (Clicking button ON) the device operating environment was uploaded. This was the prerequisite step to connect the application to the controller. The interface could be divided in four parts: motion parameter controls, motion displays, scanning parameters and limits, motion controls, Figure 3.17.

The motion parameter controls were used to fix such parameters as a velocity and an acceleration of the motion for each axis. The current position and the movement of the tables were reflected on two displays. The central display showed the XY plane of

motion and the small one was used to monitor the height. The intersection of two green lines on the XY-display determined current position of the CPD probe. The units for the table positions were in mm.

From the main window, the user also could execute basic movements of the tables and defined scanning boundaries and parameters. The “E-stop” button was used to immediately kill the motion on all axes and the “Home position” button returned all axes to their original points. The "Zero Pos" was used to fix a reference point. For the scanning routine the user could specify a starting point, an ending point and a number of steps for each axis. For convenience there is an option to set the current position as a boundary point. The averaging control was used to define how long the CPD probe stayed in each position during the scanning. The screenshot of the wire diagram of this module is shown in Appendix B.

Data acquisition software module

The DAQ module was used to monitor signals from different components of the experimental setup. The module interface contained channel controls, a trigger control, acquisition parameters controls, filtering and averaging controls. After choosing the DAQ channels the user could observe the signals from these channels on the display simultaneously and in real time. The user could set the sampling frequency and the number of data points as well as filtering and averaging settings. DAQ GUI allowed the observation of the offset, phase, shape, amplitude of the signal before a scanning procedure. A screenshot of the module user interface is shown in Figure 3.18.

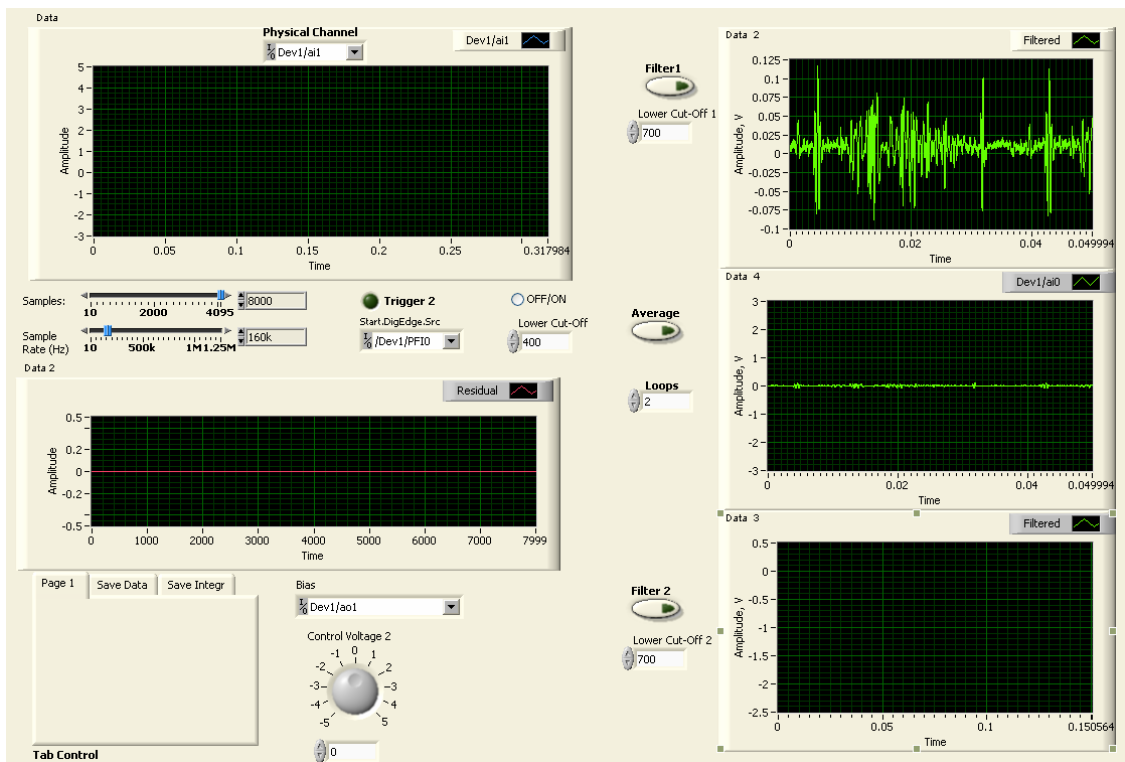


Figure 3.18: DAQ module GUI.

Some of the elements of this module were used in the other parts of the application where data recording or signal monitoring was required. The wire diagram of the common signal recording block used in this application is shown in Appendix B.

Voice Coil Control software

The Voice Coil Stage was fully tested and tuned at the factory to operate properly. The software package "Composer" was provided by system manufacturer, Figure 3.19. The Composer is a suite of software designed to enable a user to set up and fine tune motion control systems. The Composer was used to tune and test the system, to modify

the test parameters, to evaluate the closed-loop performance for the system and to edit a user program.

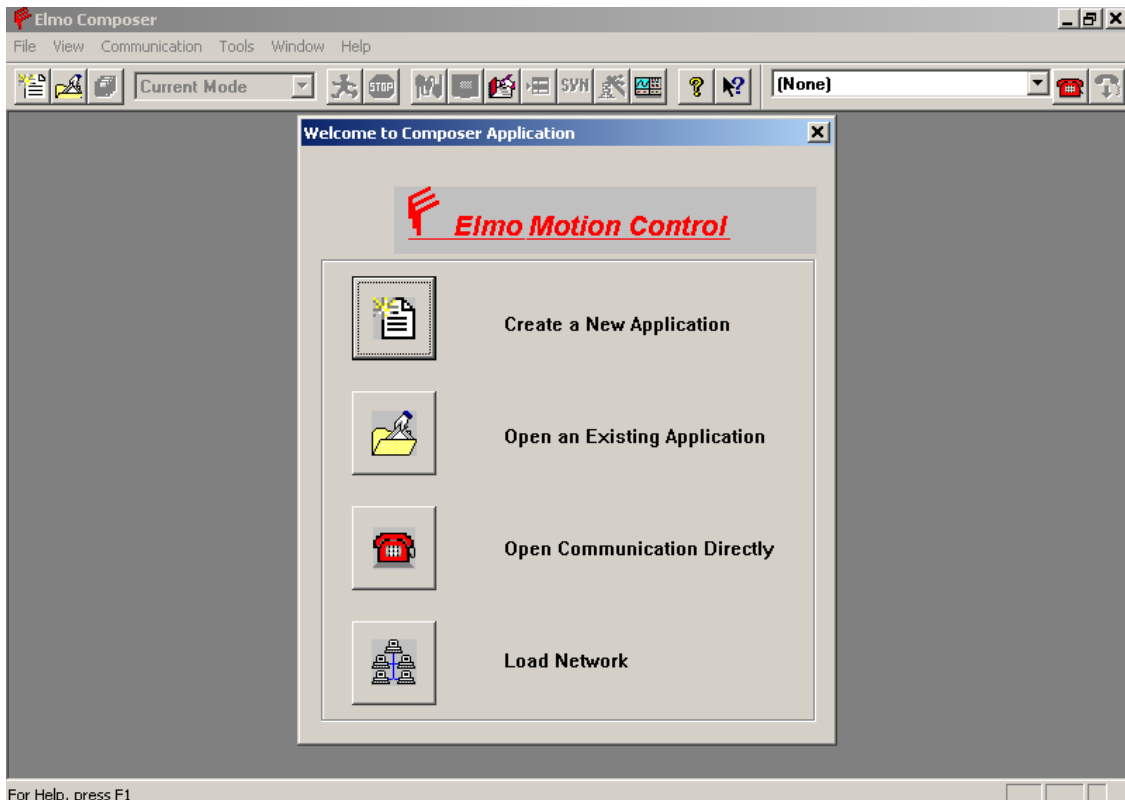


Figure 3.19: The Welcome to Composer Application window.

The Composer included a range of tools for setting up the system. Here are some of the tools that were used during the research:

- The Composer Wizard. It analyzed the entire system and defined all resonance and mechanical parameters.
- The Smart Terminal, used to manually manipulate the drive.
- The Motion Monitor, used to record and display almost any system value.

- The Elmo Studio, an environment for writing, downloading and executing programs in the connected drive.
- The Scope displayed recorded parameters and had a wide range of mathematical functions to manipulate the recorded data.

To manipulate the drive software commands were used. There were two ways to send commands to the drive: RS-232 Serial using Smart Terminal tool and a user program. Smart Terminal was used during turning, calibration and testing the system. In this case commands were typed in manually, one-by-one and an immediate response from the voice coil was observed. Afterwards Elmo Studio Program Editor, Figure 3.20, was used to write a code for a start-up program.

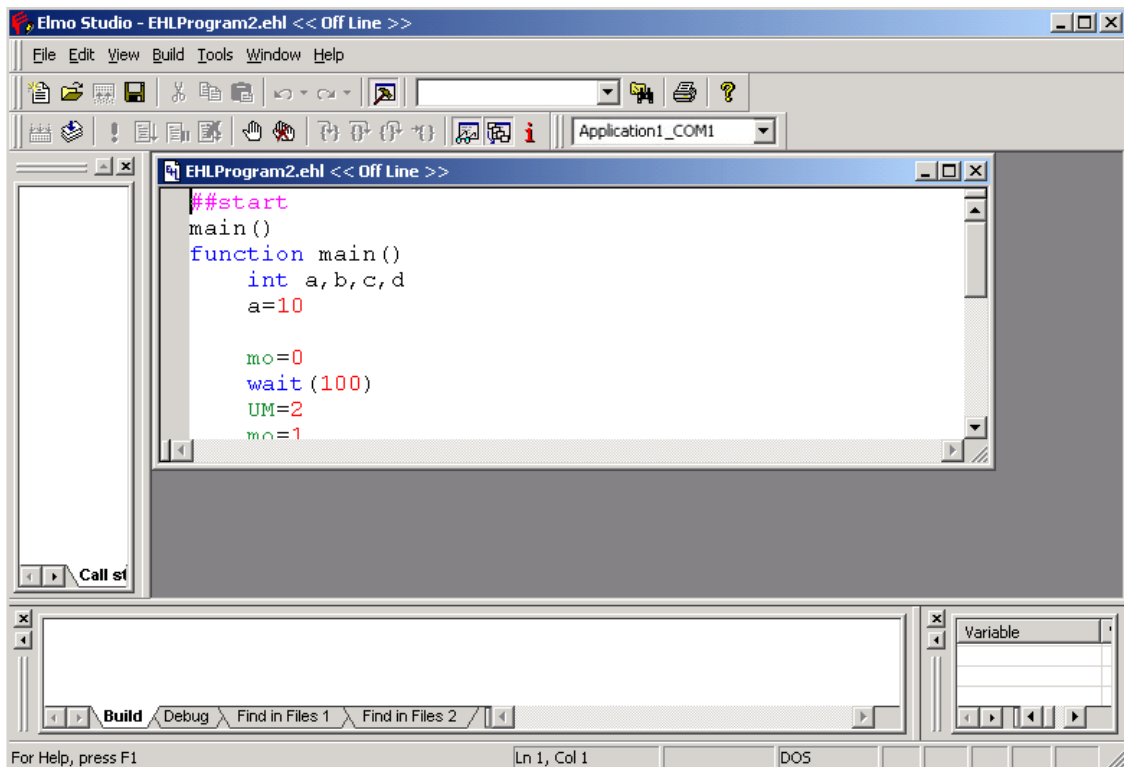


Figure 3.20: ELMO Studio - coding environment.

The start-up program (EHL file) was compiled and uploaded to the drive and started executing when power was applied. It run in an infinite loop and stopped by turning off the power to the drive or through the Composer, or by fulfilling the condition in the loop to terminate the execution. This program was used during the experimental scanning procedure. The complete program code with comments can be found in Appendix B.

More detailed information about certain software modules reviewed above is given in the next chapter in connection with the description of the experimental procedure.

CHAPTER 4

EXPERIMENTAL PROCEDURE

This chapter describes the experimental procedure and steps taken to prepare for experimental data acquisition. In order to start experiments, some preparation steps had to be done to the setup. The most important steps that influenced the quality of the results were grounding, calibration and sensors mounting.

System Preparation

Grounding

One of the biggest problems during the experiments was the noise observed in the CPD signal. The CPD sensor is a very sensitive electronic device that picks up even weak parasitic signals from surrounding equipment (the position table motors, the rotating spindle, the voice coil, the power supply, etc.). The presence of 60Hz noise and random peaks caused by positioning system motors in the CPD signal was solved by grounding of the experimental setup. All wires utilized to connect different devices were shielded with a tin-plated copper braid and grounded. The CPD probe was shielded with a frame covered with aluminum foil and grounded as well. To prevent ground loops, all signal and device grounds went to one common point on the test platform, Figure 4.1.

For the spindle 2 Amp leaf-type carbon brush was used to minimize the source of noise. These steps significantly reduced the background noise to a level of less than 10 mV.

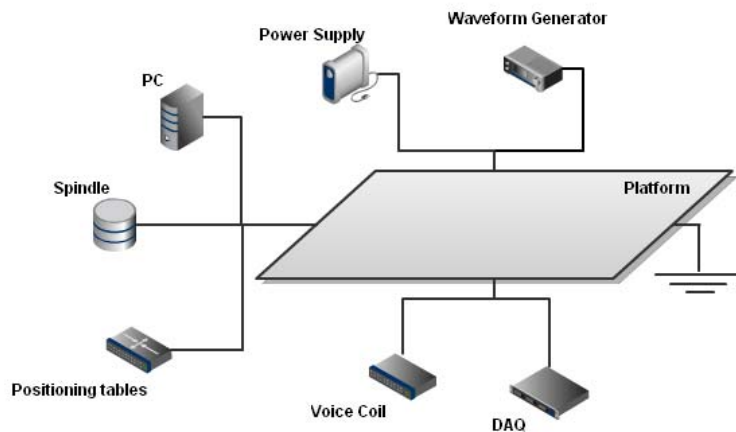


Figure 4.1: Setup grounding.

Calibration

The next step in the system preparation was calibration. Firstly, the MTI-2000 distance sensor was calibrated. The calibration was required to take into account the reflectivity of the sample surface. The calibration procedure was provided by manufacturer and was accomplished by placing the probe above the sample surface and by searching the optical peak which was described in the previous chapter, Figure 3.10.

After mounting the distance sensor on the Z-table of the positioning system above the sample surface the following manipulations were undertaken for the calibration:

1. “Range 1” was selected on the control panel of the unit.
2. The MODE switch on the right side of MTI-2000 front panel was set to “CAL”
3. Using the front panel button “Volts/EU” the front display was set to the voltage level generated by the return signal to the sensor.
4. Using the software motion control module the distance sensor was slowly raised or lowered until the voltage signal on the front panel of the unit reached its maximum (optical peak on the response curve, Figure 3.10).
5. The button "Cal Set Point" on the front panel of the MTI-2000 was pressed to complete the calibration.
6. The calibration routine was complete when "Cal in Progress" LED went off.
7. The MODE switch was set to "Displacement".
8. The sensor was lowered towards the sample surface until the output voltage was around 3-4V, which corresponded to the middle point of the working range 1 on the response curve, Figure 3.10 (front slope).

After the MTI-2000 calibration it was necessary to calculate a transfer coefficient used in the start-up program uploaded to the voice coil controller. This coefficient was utilized to convert the voltage control signal from the distance sensor to the corresponding number of steps that were passed to the drive to shift the voice coil. First the coefficient was theoretically calculated, as shown in Equation 4.1, then adjusted and validated by experiment.

$$N_{st} = \frac{V_{control} \cdot \text{Sensitivity_of_module}}{\text{Translation_module_resolution}} = V_{control} K_{tr} \quad (4.1)$$

Where

N_{st} is the number of motion steps,

$V_{control} = V_{cur} - V_0$ is the difference between the output voltage of distance sensor in the current position and the voltage in the initial point,

K_{tr} is the transfer coefficient.

The MTI-2125H probe module was utilized during the scanning procedure therefore all calculations were based on its parameters. Sensitivity of the module and resolution of the translation module were $0.33 \frac{\mu m}{mV}$ and $5 \mu m$ respectively. The sensitivity units were converted to $\frac{\mu m}{V}$ and the transfer coefficient was calculated using Equation

4.1:

$$K_{tr} = \frac{\text{Sensitivity_of_module}}{\text{Translation_module_resolution}} \cdot \frac{1000 \cdot 0.33 \frac{\mu m}{mV}}{5 \mu m} = 66 \quad (4.2)$$

To validate or correct this value an experiment was conducted where other probe module MTI-2032R was mounted on the voice coil and placed above the sample surface. In close proximity to the coil the MTI-2125H probe was mounted on Z-axis table of positioning system, as shown in Figure 4.2.

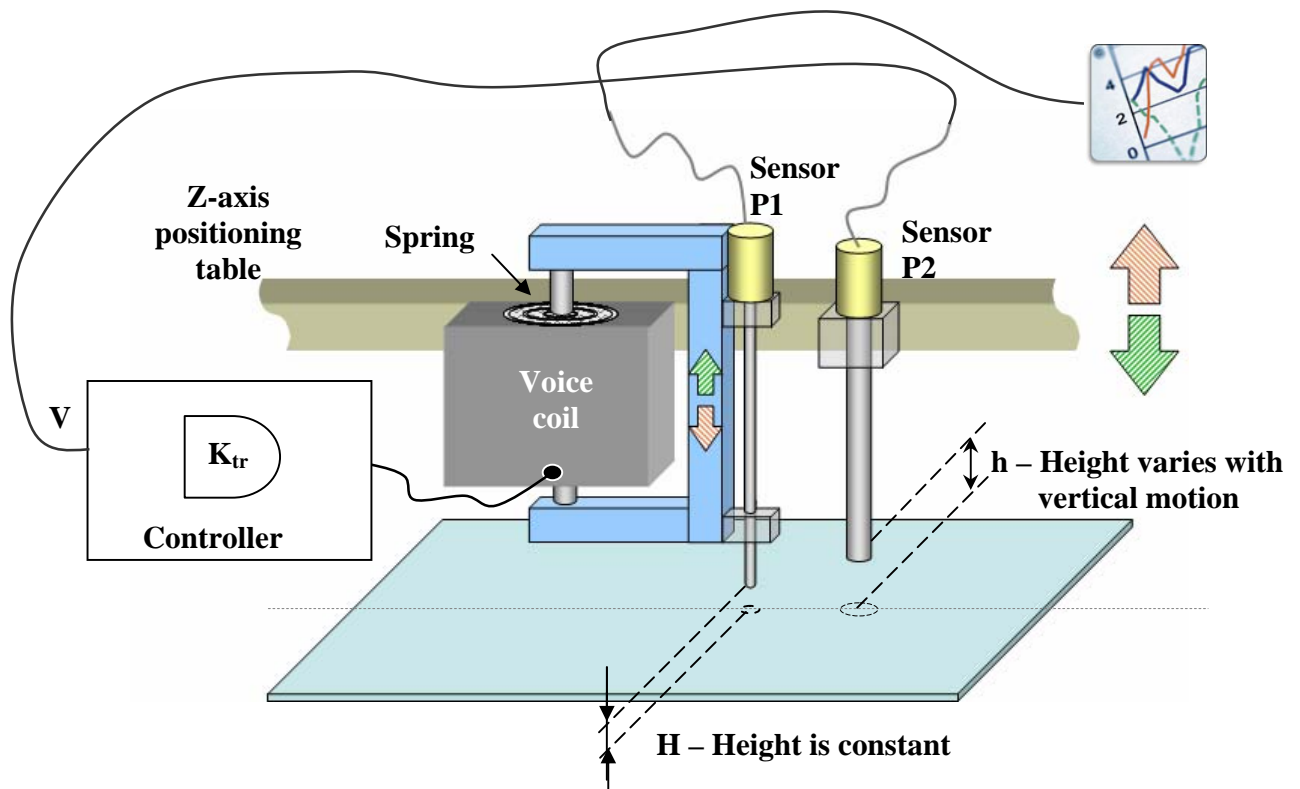


Figure 4.2: Transfer Coefficient correction experiment.

Using the software motion control module the Z-axis table was slowly raised or lowered. The probe P2 measured the displacement and its output voltage was passed to the coil controller. The controller program then used this voltage and the transfer coefficient as parameters to calculate the travel distance for the voice coil actuator. In an ideal case the actuator would move the same distance as the Z-axis table but in the opposite direction (compensate the displacement) so that the gap between the probe P1 and the surface would be constant. P1 probe was used to control the quality of the voice coil response with a specific transfer coefficient. Corrections to the coefficient were made

based on the P1 output curves that are shown in Figure 4.3. It can be observed that the best result was achieved with the coefficient of 64.3.

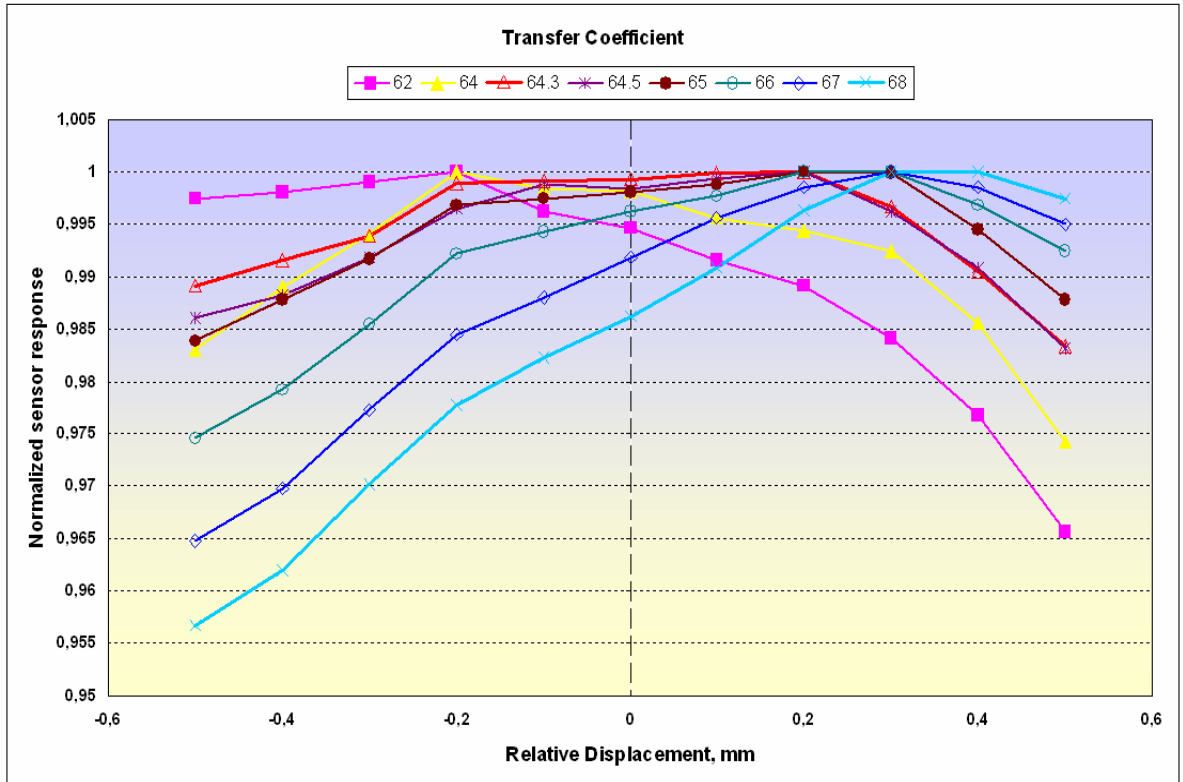


Figure 4.3: Voice coil actuator response for different transfer coefficients (normalized).

Mounting

Proper mounting and alignment of the CPD sensor and the distance sensor was very important for the experiment procedure. The initial plan was to place the sensors at different points of the same track, Figure 4.4a. Such separation would allow the voice coil to immediately react to the variation of the profile measured by the distance sensor during a single track scan. However this approach would bring an additional complexity

to the scanning procedure such as the need to shift an analog signal to a certain phase before passing it to the voice coil controller.

To simplify the process and avoid possible synchronization errors it was decided to align both sensors along the Y axis, Figure 4.4b. In this case one extra scan was needed to record the track profile first and then use it as a control signal for the voice coil during CPD data acquisition. Detailed information about this procedure is presented in the next section.

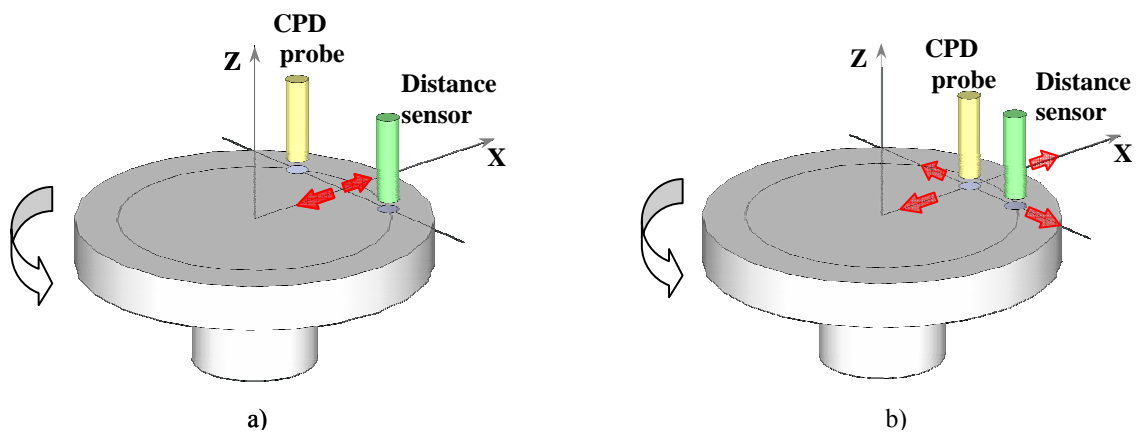


Figure 4.4: CPD probe and distance sensor mounting.

Wafer Sample

A lot of auxiliary wafer samples, mostly hard drive platters, were used during the research to test the experimental setup. But for the final experiments a silicon wafer substrate and thin metal films (Au, Ti) deposited on it was used, Figure 4.5.

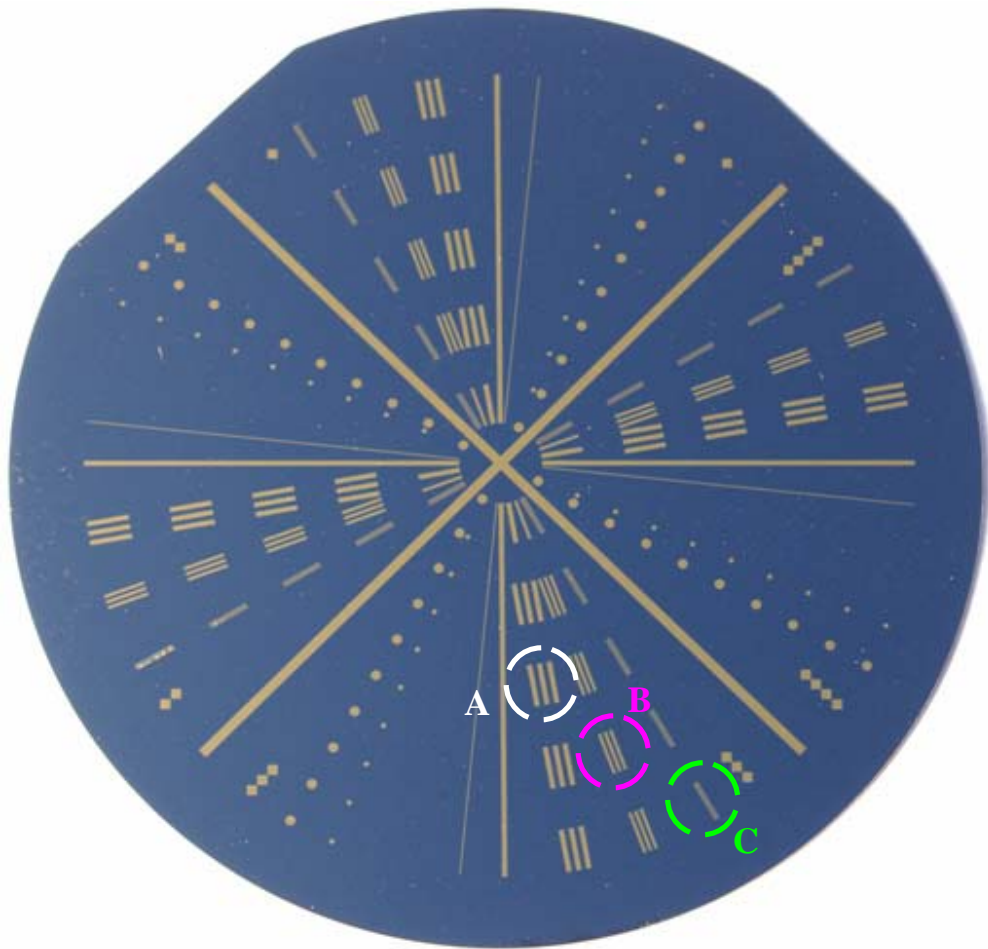


Figure 4.5: Wafer Sample with Au and Ti films. Film width: A -500 micron, B-300 micron, C-100 micron.

The lines and dots are the sputtered metal films. The line width and the space between lines (A, B, C in Figure 4.5) were known so this allowed an ability to estimate and compare the resolution of the CPD probe under different experimental conditions.

Acquisition Parameters

After the experimental hardware was set up and calibrated, it was necessary to adjust the acquisition parameters in accordance to the experiment requirements. The three important parameters related to the data acquisition process were spindle rotation velocity, sampling rate and number of samples to acquire.

The rotation velocity was controlled by the DAQ analog output using the Labview application and measured by the EE-SPX302 trigger. The sampling rate was controlled by the scanning module of the software application. The number of samples was calculated from the rotation frequency and the sampling rate.

The primary control parameters that were set using the software application are listed in Table 4.1.

Table 4.1: Typical data acquisition parameters.

Parameter	Description	Range (regular value)
Sample Rate	The rate at which DAQ hardware sampled the CPD output voltage	<i>1Hz-1.2MHz (80kHz)</i>
Rotation Frequency	Velocity of the spindle with the sample wafer to scan	<i>1-50Hz (11Hz)</i>
Digital Trigger	Enable software to initiate data acquisition based on the signal from the trigger.	<i>On/Off (On)</i>
Scan averaging	Determine if only one or multiple series of data captured for the same track	<i>On/off (On)</i>
Number of scans	If averaging is enabled determines the number of data sets to capture and average.	<i>2-100 (10)</i>

Scanning Technique

After the acquisition parameters were defined and all hardware connected, the setup was ready to perform scanning. The sample wafer was placed on the spindle, centered and fixed with 3 clips around the perimeter. The center of the wafer then was defined as the origin for the X and Y positioning tables. Distance, D , Figure 4.6, between the CPD probe and the height sensor (difference of Y coordinates) were calculated and recorded.

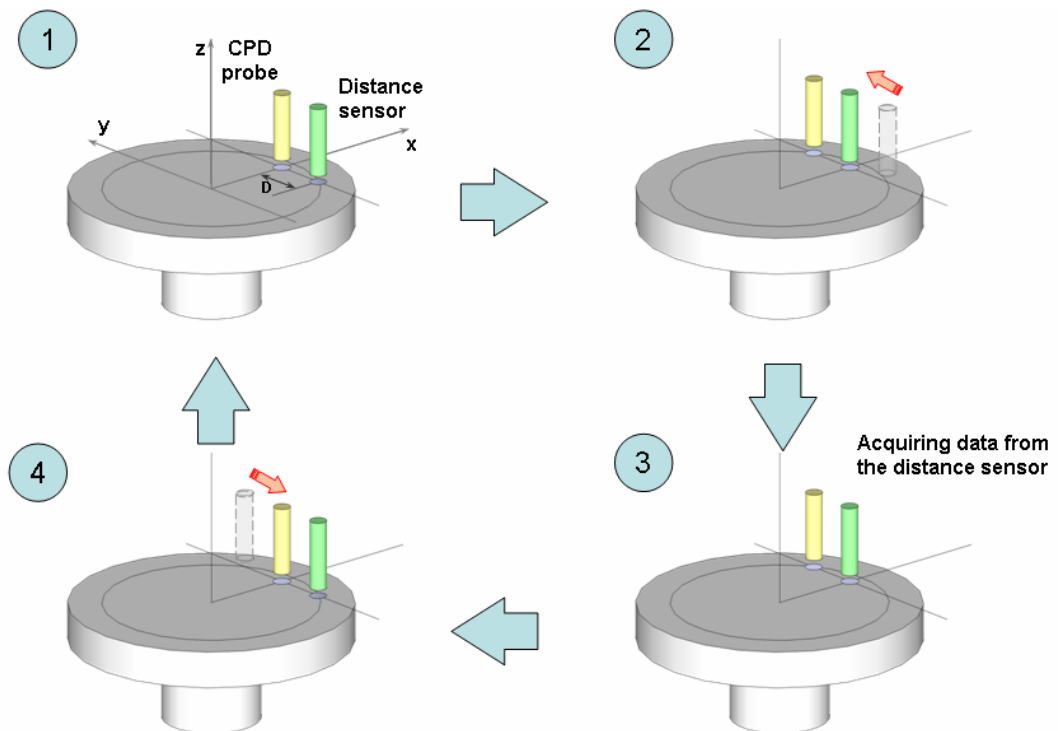


Figure 4.6: Setting the reference point for the distance sensor (spindle is static) or scanning a track (spindle rotates)

The fly height for the CPD probe was calibrated using the following technique. The probe tip was lowered until it touched the surface of the wafer. Contact was verified by the output signal from the probe, which jumped to the high level. The probe tip was then raised slowly until the probe signal was back to the original value which indicated that contact was broken. This point was assumed as 0 microns fly height. The tip was then raised to the required for the experiment fly height.

A corresponding output value from the distance sensor for this fly height was to be captured. This value was the reference point for the distance sensor which was calibrated as shown in Figure 4.6. The sensors were moved along the Y-axis to the distance D so that the previous position of the CPD sensor became the current position for the height sensor, Figure 4.6 (2). At this spot 10 data points were acquired from the height sensor and passed to the voice coil controller where the average value was calculated and saved as a parameter. Then the sensors were returned to their initial position.

The next step was to define boundaries of scanning and number of tracks to scan. Since the probe during the scanning moved along the X-axis outwards, boundaries were defined in mm as a minimal and maximal value of X coordinate. After all initial parameters were calculated and set last step prior scanning routine was to choose the path of the text file to be written.

The spindle then was turned on and when the correct rotation frequency was reached the scanning routine was started. A diagram of this routine is shown in Figure

4.7.

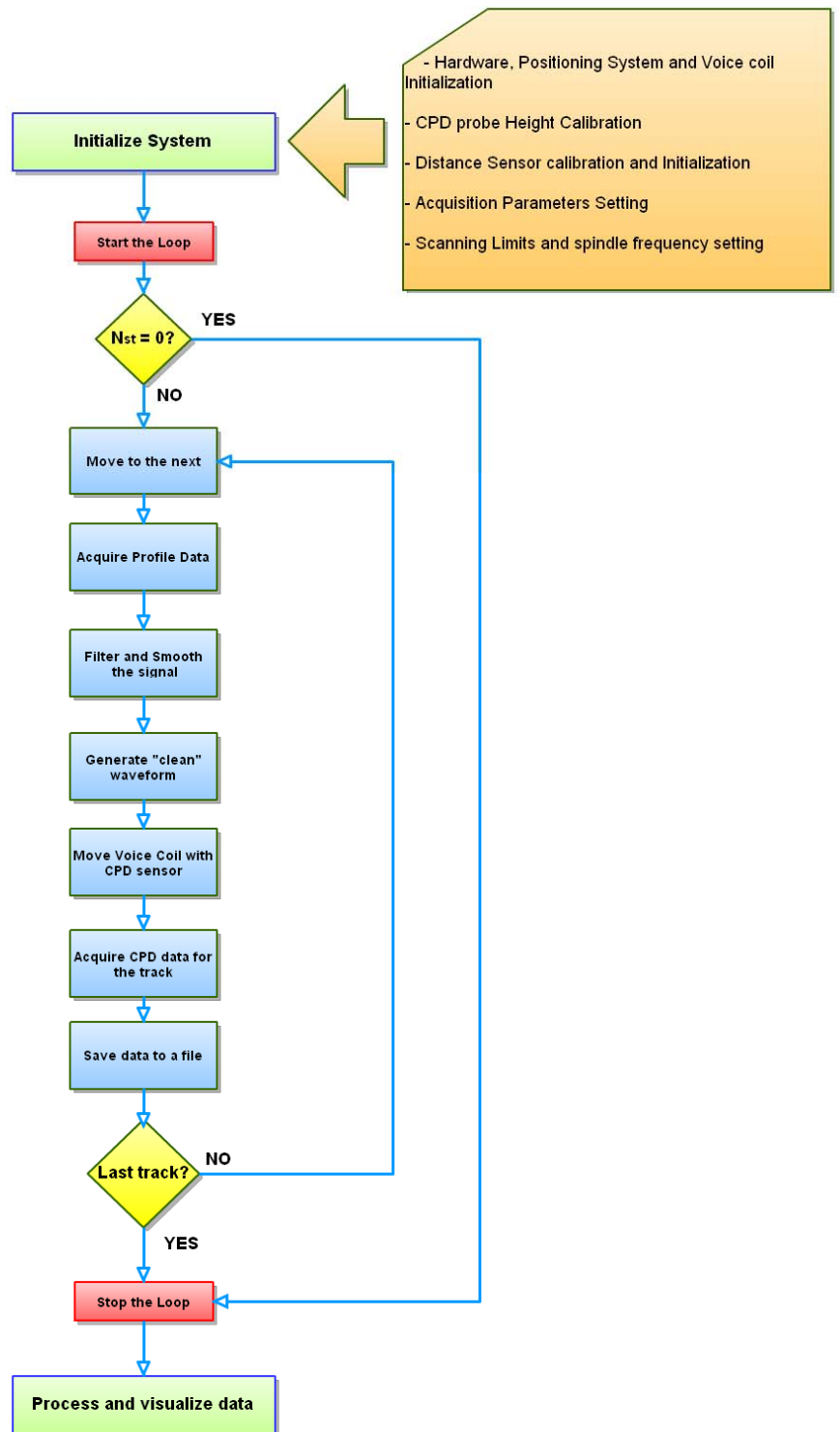


Figure 4.7: Scanning routine.

For each iteration of the scanning loop the distance sensor was placed above the track of interest (the same way as described above for the capturing the reference value for the fly height, Figure 4.6 (2-3)). The sensor output signal (track profile) then was recorded, processed and passed to the waveform generator. The generated signal was used as an input for the voice coil controller. The controller using the reference point recorded earlier computed the voice coil displacement and its direction for each point of the track. Thus, the voice coil compensated height variation between the CPD probe (mounted on the coil) and the surface. Data acquisition started when the CPD sensor placed back to its initial position, Figure 4.6 (4-1). The fact that the profile data and the CPD data recorded from the same position helped to avoid possible synchronization and alignment errors during the terrain following. Amount of data acquired for each track (number of rotations) was determined by averaging settings.

This process was repeated until the limit was reached. During the profile data acquisition and during the motion between tracks the voice coil raised the CPD probe to the safe height to avoid touching the surface.

After the desired data was collected, the file containing the results for the measurements was then processed for plotting through the written visualization module of software application. In this module results could be observed as a 3D and 2D (top view) map, single track results was processed and observed using MS Excel.

CHAPTER 5

RESULTS AND DISCUSSION

This chapter describes the experimental results. Multiple experiments were run in order to validate and ensure system performance, while other experiments were carried out to analyze improvement of the nvCPD scanning technique. Effect of fly height on the resolution was studied.

Surface profile

First, profile measurements were accomplished for the whole sample. This was needed to estimate the signal from distance sensor and visualize the surface profile. One example of the signal profile is shown in Figure 5.1.

It was observed that the profile reflected all metal features on the sample surface as sharp peaks and could not be used as a control signal for the voice coil. As was shown in Chapter 2 the signal from the height sensor had to be filtered and smoothed to represent only small, stepless variation of the surface due to incline the surface, wobbling or flatness imperfections that prevent from the scanning the surface on a desired height. For this purpose a Labview module was created. In this module the signal processing functions (Peak Detector and Curve Fitting) from Labview libraries were used. At the beginning, track data were analyzed to detect all peaks and to subtract them from the signal. Curve fitting with polynomial of order 7 was then applied to obtain a smooth

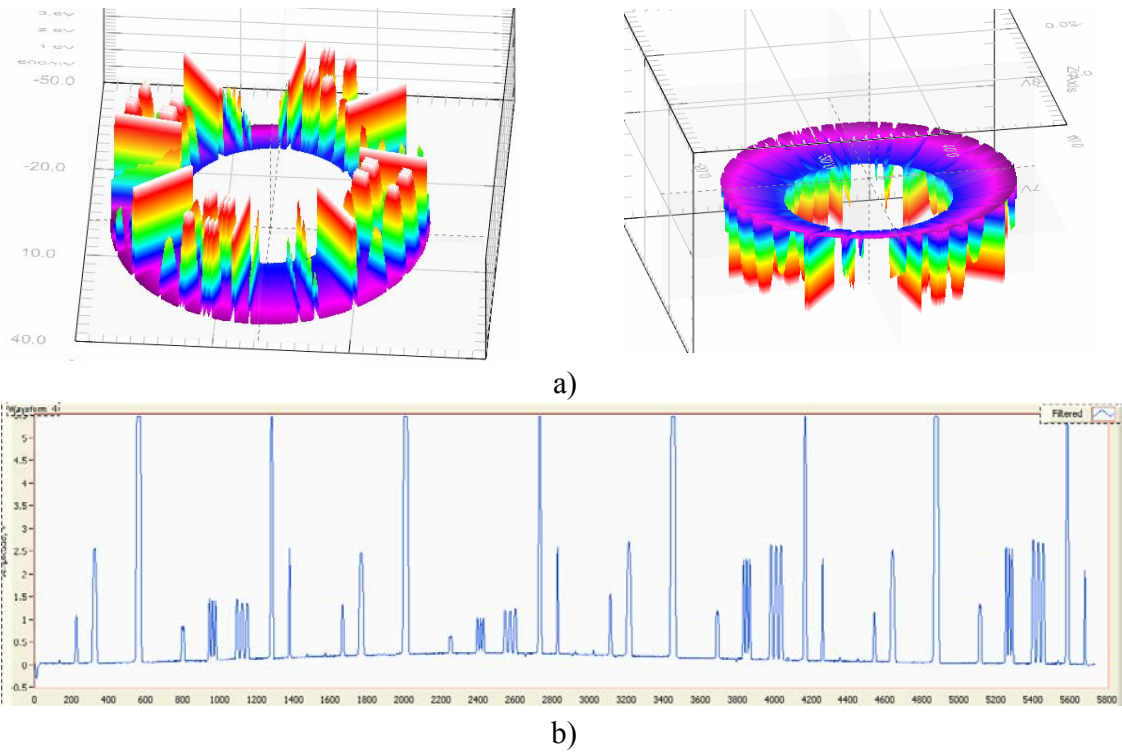


Figure 5.1: Distance Sensor: Sample Profile: a) 3D Map; b) one track profile.

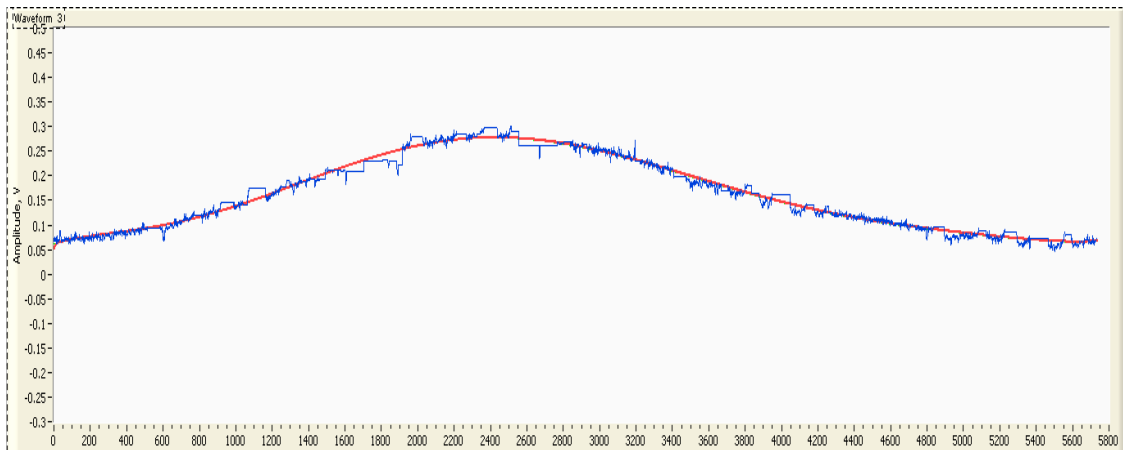


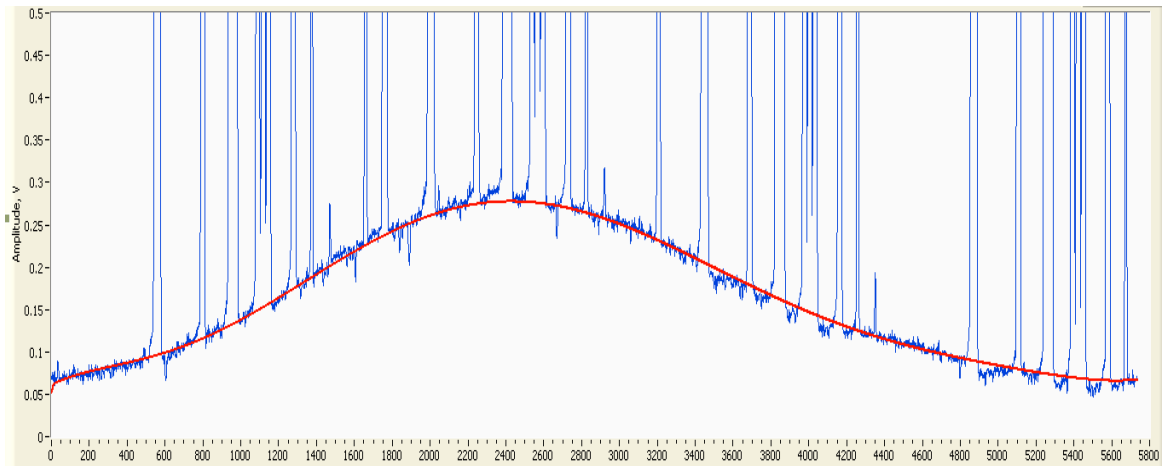
Figure 5.2: Profile data processing: track data without peaks and fitted curve.

signal, Figure 5.2. Goodness-of-fit was estimated and presented in Table 5.1 for each track of the profile.

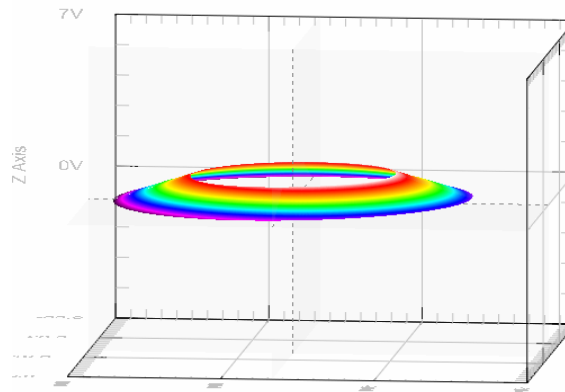
Tale 5.1: Goodness of fit.

Track #	R²
1	<i>0.951788</i>
2	<i>0.956644</i>
3	<i>0.962239</i>
4	<i>0.976793</i>
5	<i>0.936520</i>
6	<i>0.966583</i>
7	<i>0.974623</i>
8	<i>0.954642</i>
9	<i>0.962501</i>
10	<i>0.964998</i>
11	<i>0.976107</i>
12	<i>0.956367</i>
13	<i>0.962868</i>
14	<i>0.980890</i>
15	<i>0.978980</i>
16	<i>0.976806</i>

Figure 5.3 shows the initial signal from the height sensor and fitted curve and filtered and smoothed 3D surface profile.



a)



b)

Figure 5.3: a) Track profile and fitted curve, b) filtered profile surface.

Static nvCPD probe scanning

To estimate the improvement of the new scanning technique and to compare the results from different techniques experiments were conducted on the same wafer. To simulate a flaw during the scanning the platform with the sample was inclined at an angle of 1.5 degree from the vertical axis, Figure 5.4.

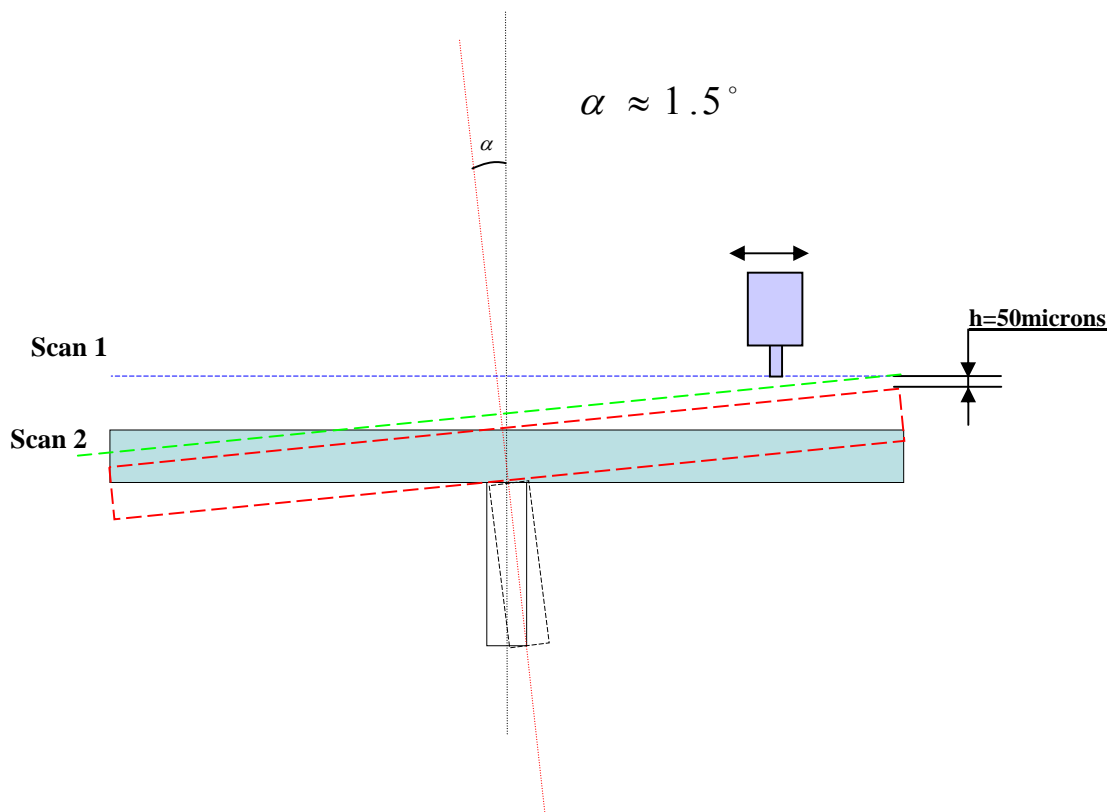


Figure 5.4: Incline of the sample.

Firstly, classical nvCPD scanning technique (fixed fly height) was used to obtain the CPD image of the surface. Since only lateral resolution is important for this scanning technique the radial step was relatively large and set to 0.5 mm but the sampling frequency was set to the value (80kHz) that gave the lateral resolution on the biggest radius in the order of 30 microns/sample. The big radial step allowed decreasing a file size and speed up the data processing. The fly height at the closest to the CPD sensor point was set to 50 microns. A CPD image of the wafer is shown in Figure 5.5.

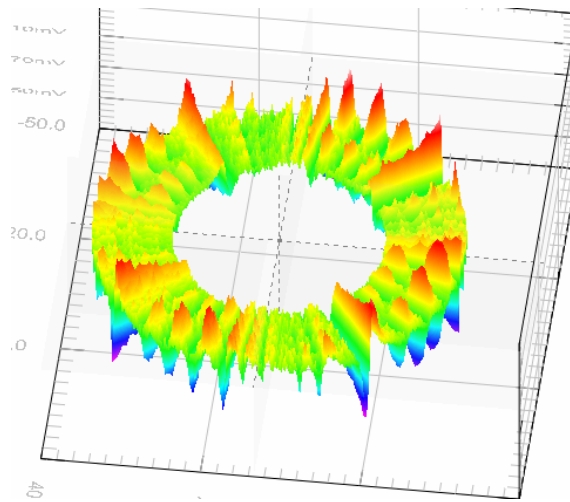


Figure 5.5: Wafer image taken using the classical nvCPD technique: 3D map.

The features were detected by the nvCPD sensor and displayed on the 3D map with different intensities and contrasts. The CPD signal intensity was the voltage change measured by the probe at the silicon substrate-metal region. Signal strength could be extracted from a track line data, Figure 5.6.

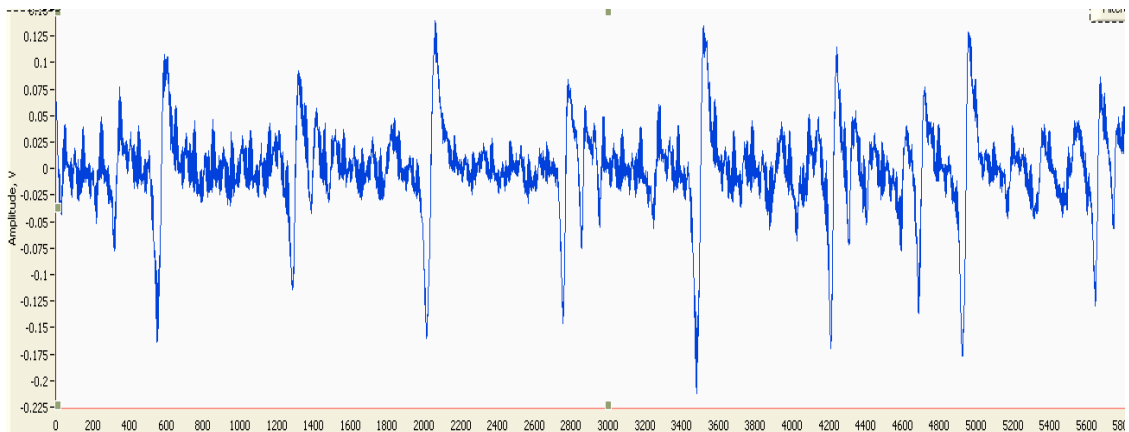


Figure 5.6: Track profile data.

It is important to note that the signal strength changed with the track radius. It was due to fly height variation along the radius and the linear velocity under the CPD probe tip as well, Equation 2.15.

Dynamic nvCPD probe scanning

After static nvCPD scanning the same wafer was scanned using the terrain following technique. A CPD images of this scan is shown in Figure 5.7.

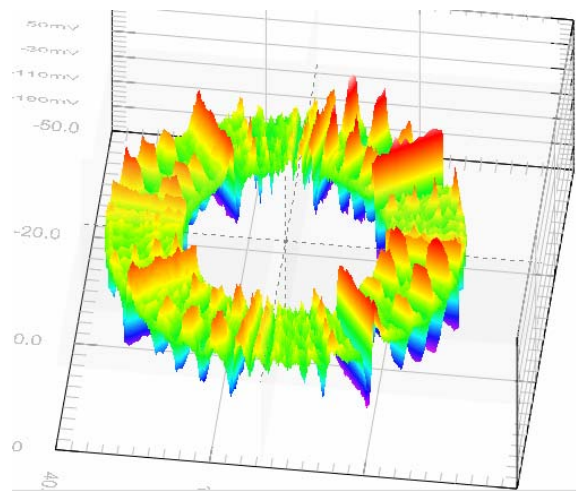


Figure 5.7: Wafer image taken using the dynamic nvCPD system: 3D map.

It needs to be noted that during this procedure the fly height was adjusted not only before track scanning (to compensate incline) but also during motion above a track since the fly height variation between the track and the sensor existed as shown in Figure 5.2. From this figure it is easy to see that central part of the track was the farthest from the CPD sensor. Thus signal was weaker and signal to noise ratio smaller. But as shown

in Figure 5.8 for the second run, where the fly height was relatively uniform along the whole track, the central peaks increased amplitudes what noticeably improved the signal to noise ratio.

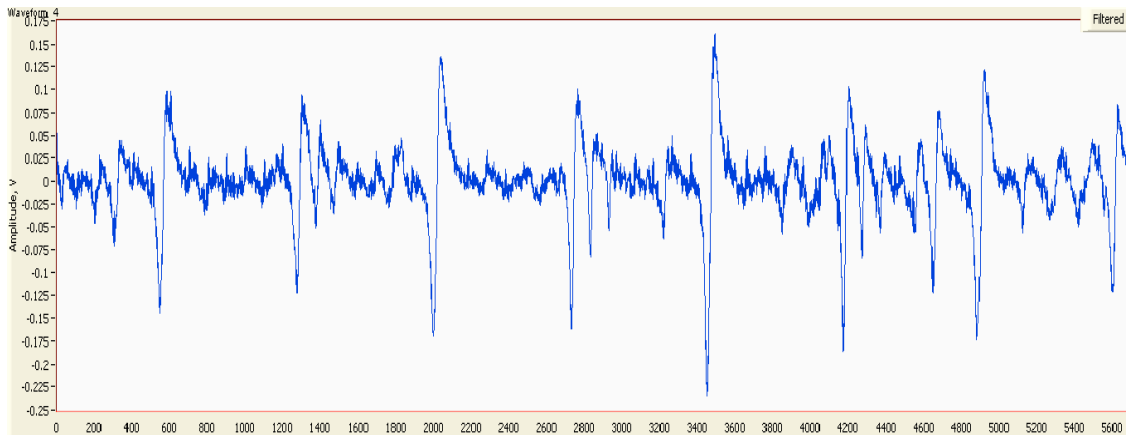


Figure 5.8: Track profile data.

Result comparison

Figure 5.9 displays results obtained during the surface scanning while using (a) static nvCPD probe and (b) the new terrain following technique.

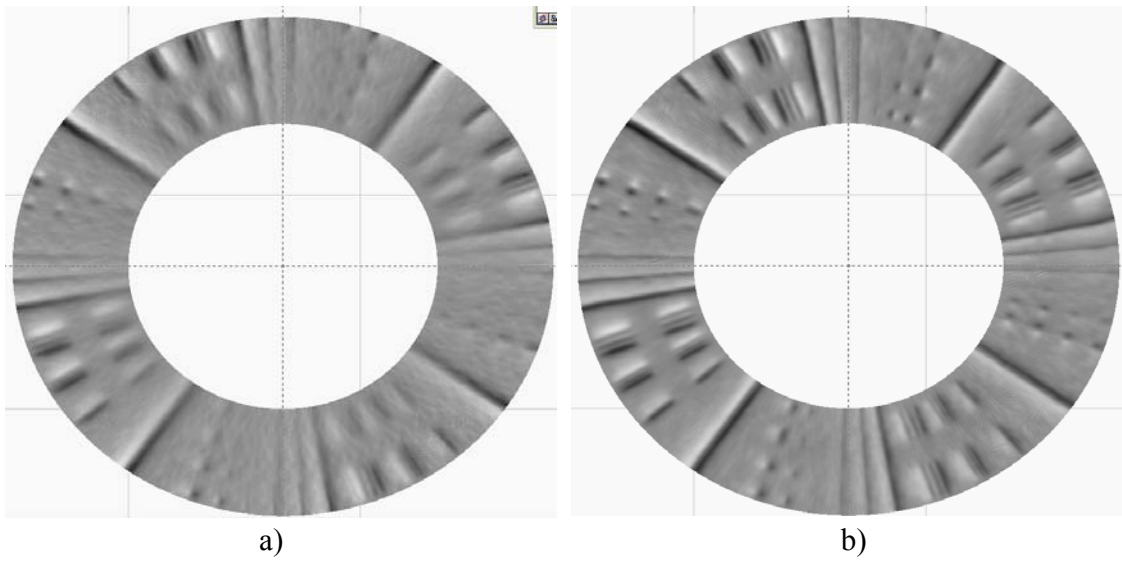


Figure 5.9: Wafer images taken using both techniques: a)static nvCPD probe technique;
b) terrain following technique.

Visual inspection of these images can detect significant improvement in the signal-to-noise ratio and as a result in the resolution of scanning for the new technique. Signal from some features after static nvCPD probe scanning was on the level of noise so the contrast with background was very low. This was due to the signal amplitude decrease as the fly height increased.

Detailed analysis was applied to individual tracks to quantitatively estimate the improvements. The inner radius track signal is shown in Figure 5.10 for the both techniques.

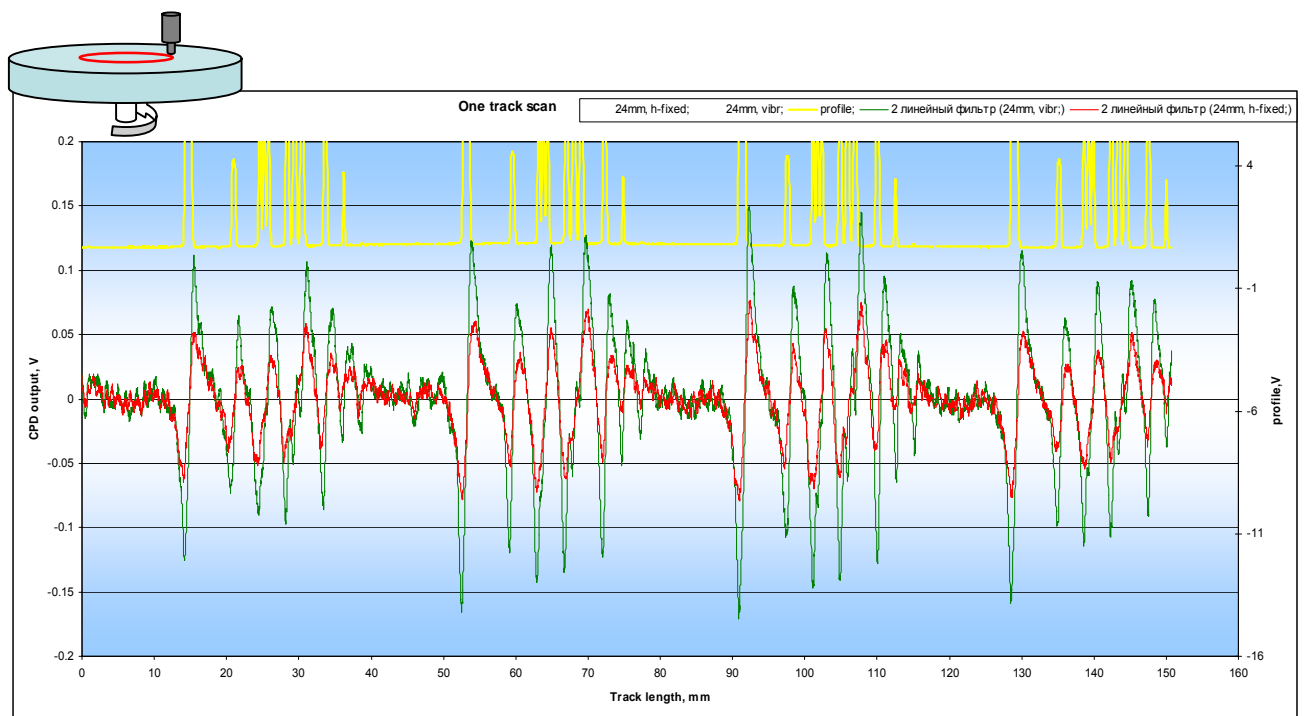


Figure 5.10: Inner radius track.

Full-Width Half-Maximum (FWHM) technique was used to describe the measurement since peaks in the signals did not have sharp edges. Using this technique a full width of a peak is measured at a half of its amplitude. It is a simple and well-defined number which can be used to compare the quality of signals obtained under different conditions. One set of peaks were chosen from two tracks to calculate the amplitude and width ratios, Figure 5.11.

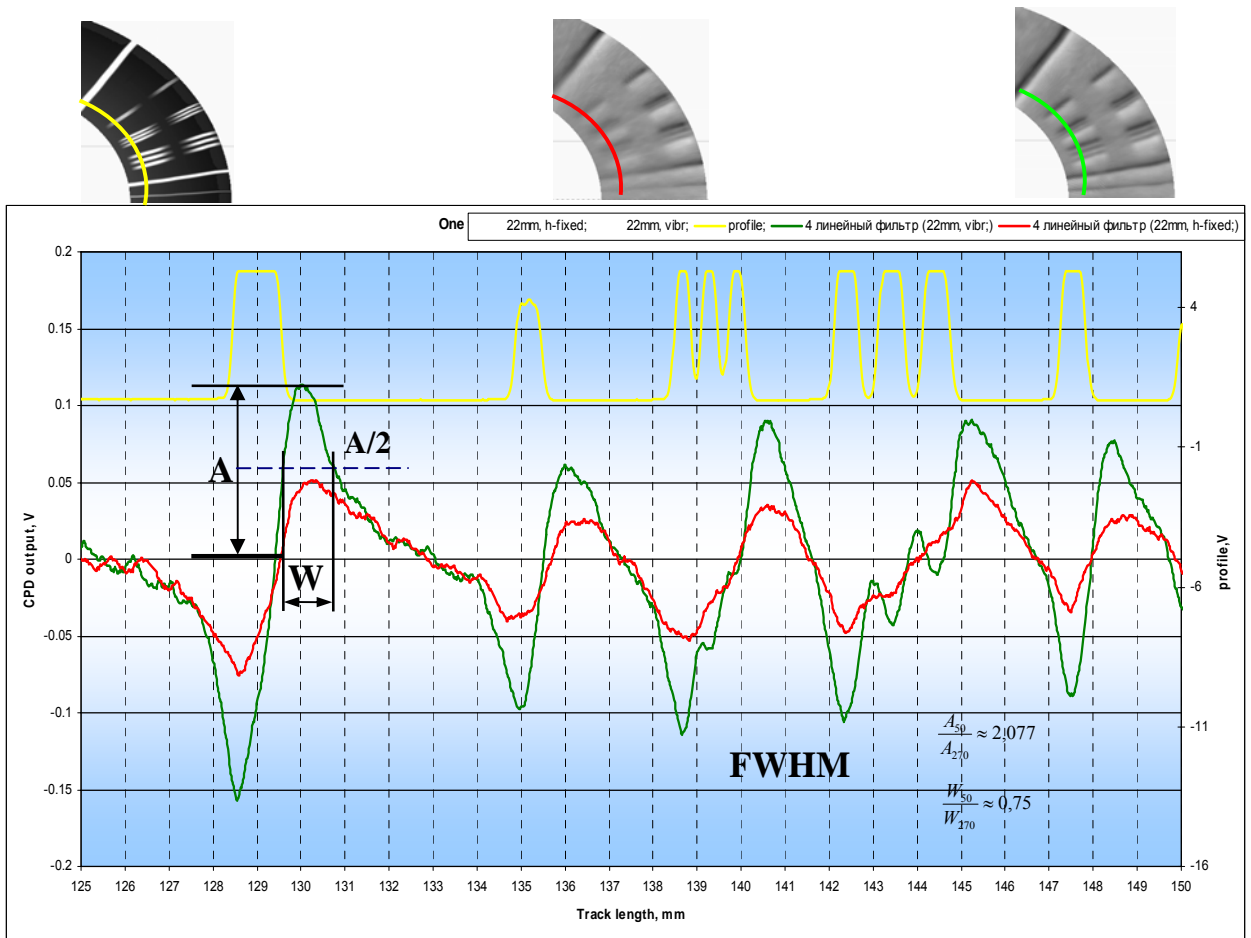


Figure 5.11: Inner radius signals fragment with peaks.

For the static nvCPD probe, scanning fly height was 270 microns for the given peaks fragment, while for the new technique fly height was set to 50 microns for the whole surface. Amplitude ratio showed that for the improved technique signal magnitude was increased by 100% and width ratio indicated that the peaks were sharper and steeper. The decrease of width by 25% could be explained by the change of effective area of the probe: the closer the probe tips are to the surface the smaller the effect of the fringe field.

These improvements in the contrast of the signal and the lateral resolution was reflected on the CPD image, Figure 5.9b, where metal features can be recognized easily in comparison with Figure 5.9a.

The same calculations were made for the outer radius of the surface, Figure 5.12 and Figure 5.13. For the static and dynamic nvCPD probe scanning fly heights for the presented fragments were 100 and 50 microns correspondingly.

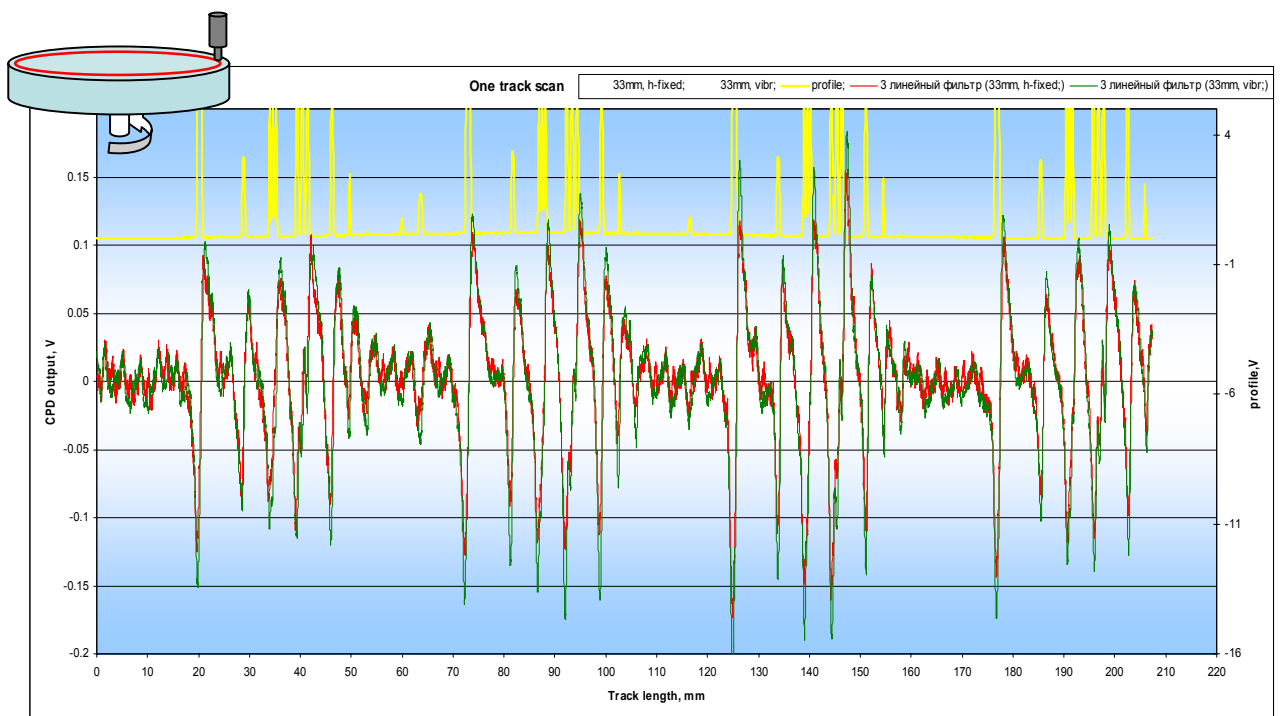


Figure 5.12: Outer radius track.

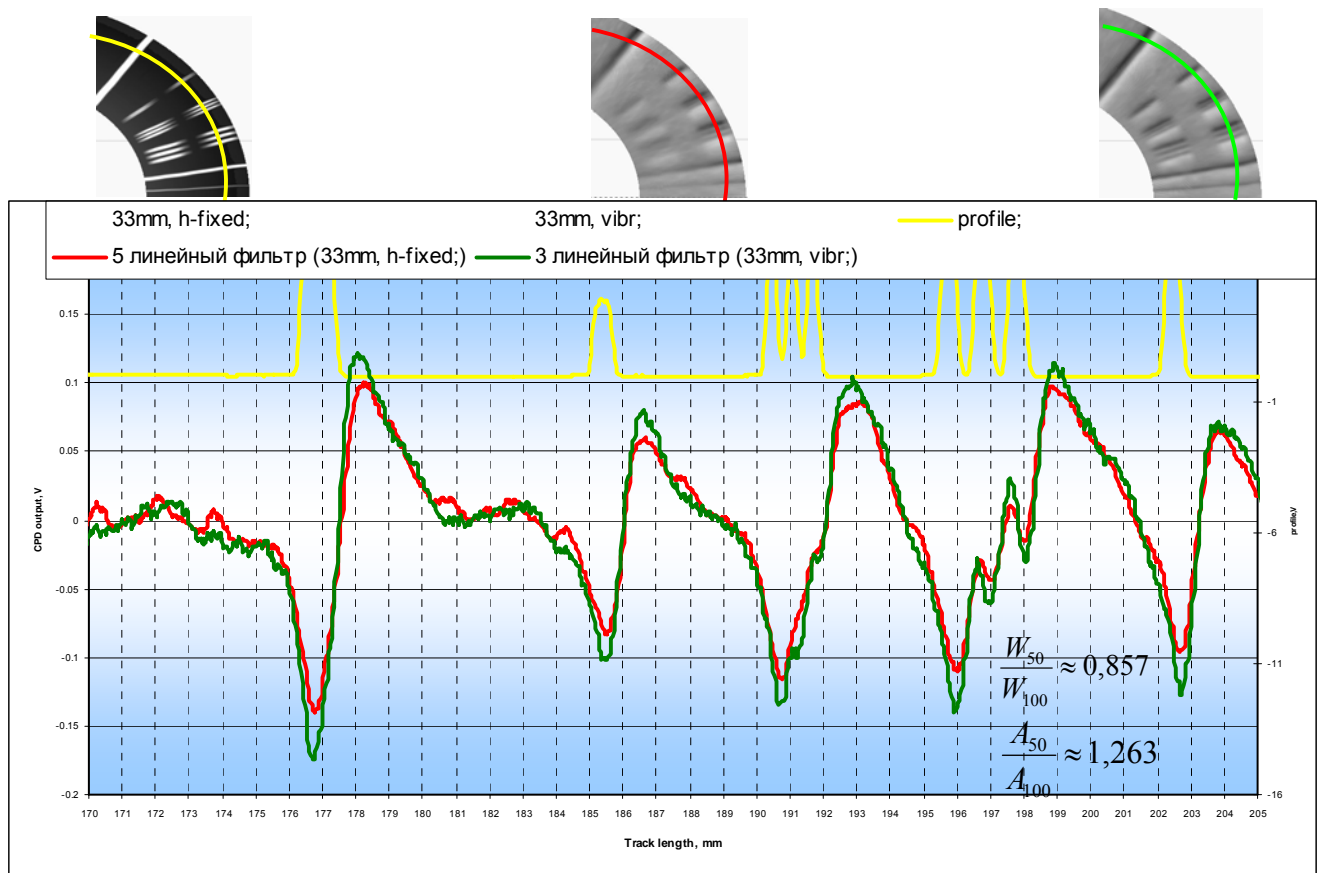
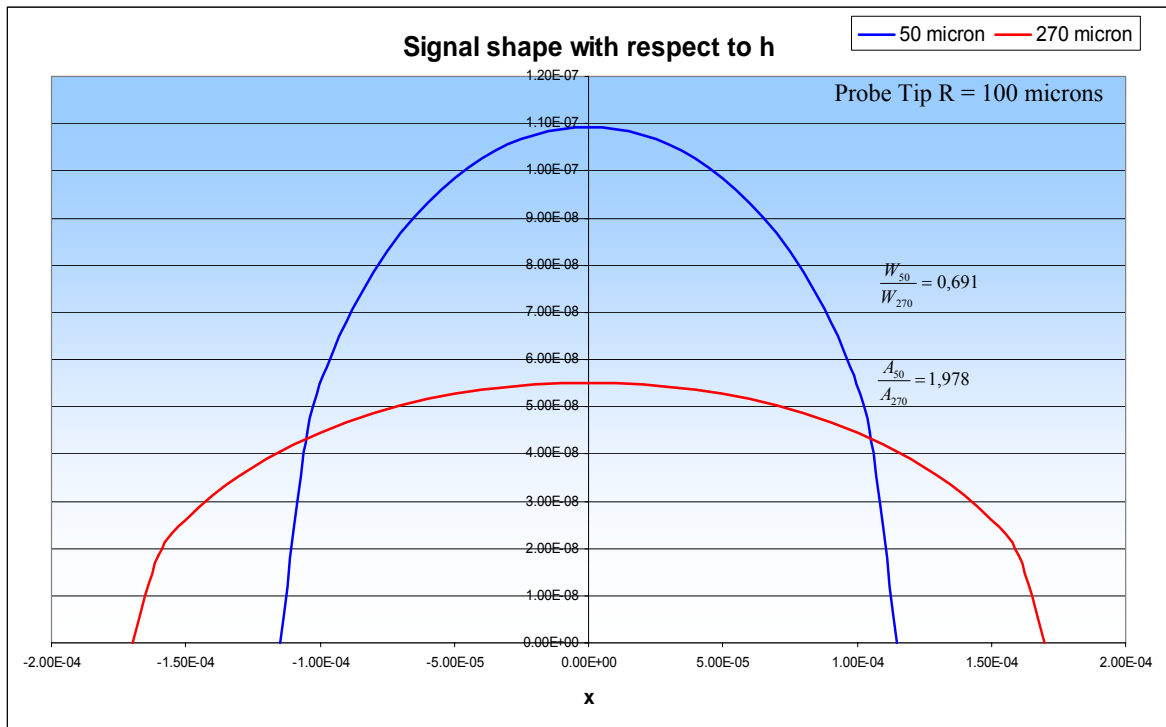


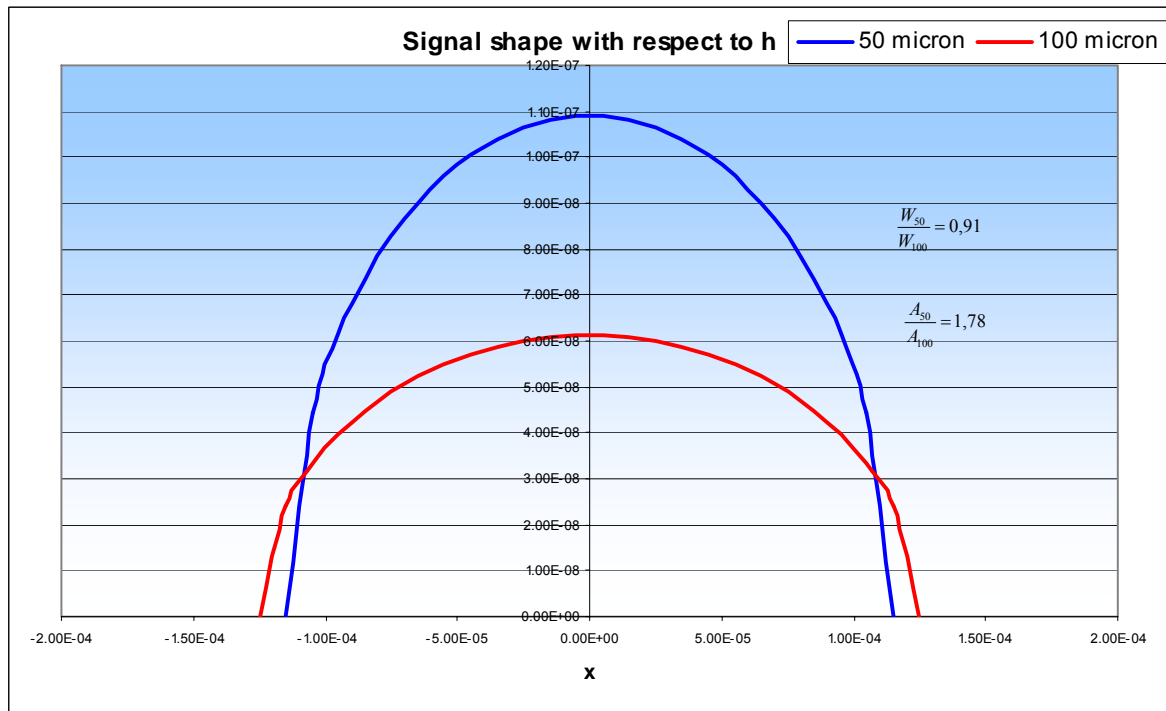
Figure 5.13: Outer radius signals fragment with peaks.

Comparison of Response Model with Experimental Results

The presented results were compared to the results from the model described in the Chapter 2. Figure 5.14 displays the shape of the signals calculated using the fly heights from the experiments and the CPD probe tip radius as an input parameters.



a)



b)

Figure 5.14: Theoretical results for a) inner radius track, b) outer radius track.

The data from the model did not show the absolute value of the signal but allowed to estimate the change of the signal due to fly height and CPD probe effective radius variations.

Effect of Fly Height on response

During the research it was observed that for the nvCPD scanning technique a fly height had to be considered in connection with a probe tip size or a probe tip effective area to achieve better results. In the Chapter 2 the CPD probe response was described and linear dependence from ratio A/h was derived. Figure 5.15 shows that the choosing of the right relation between the probe area and the fly height can improve signal to noise ratio and resolution of measurements significantly.

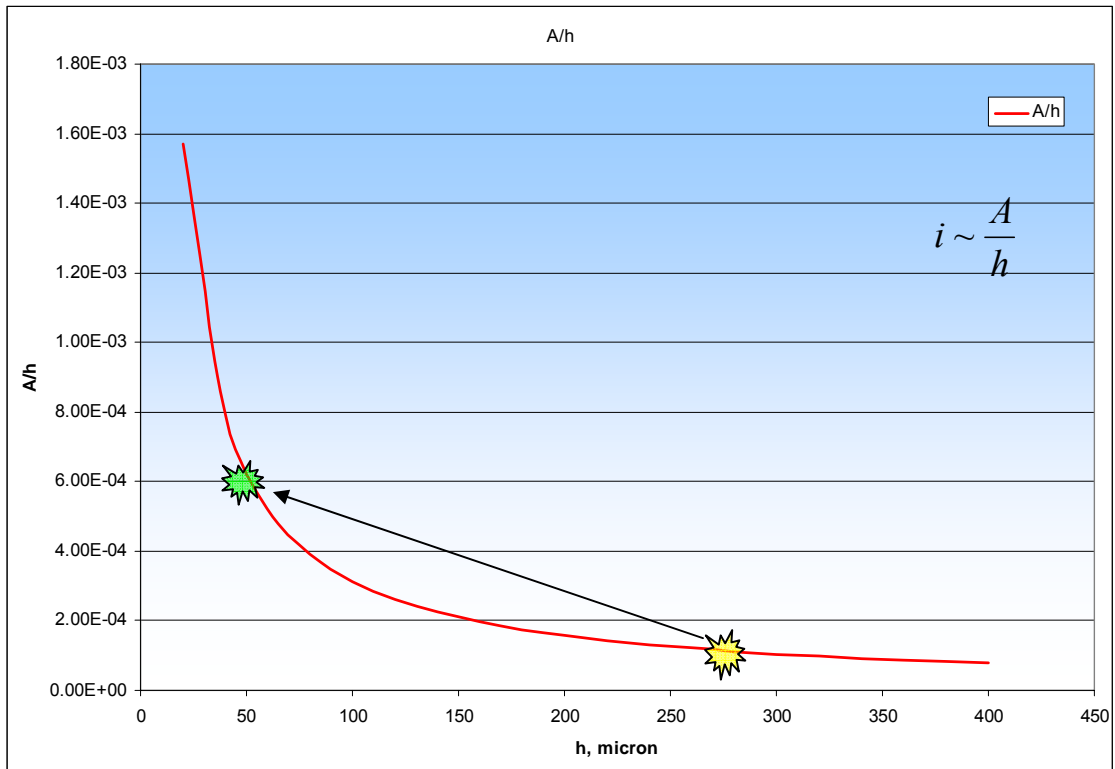


Figure 5.15: CPD Probe area and fly height correlation.

As an example, points at which inner radius track was scanned using both techniques are marked. This clearly shows that for the given probe size the change of the fly height brought the measurements to the point where even small height variation would cause big changes in A/h ratio and as a result in CPD probe output.

The results displayed in this section are the main contribution of this thesis to the proof of concept of terrain following in nvCPD scanning. It was proven that not only difficulties arisen during the nvCPD scanning technique can be overcome but scanning of non-planar surfaces can be successfully accomplished. Further improvement and variation of setup components are required in order to achieve real time performance and expand the boundaries of the technique application.

CONCLUSION

Non-vibrating contact potential difference probes provide rapid measurements of work function variation over a surface. This research shows that nvCPD scanning technique can be improved to overcome difficulties arisen during the scanning and to expand application limits of this method.

Terrain following improvement was presented. This allows controlling and adjusting dynamically the fly height during the scanning. Since the signal is inversely proportional to the fly height minimization of this parameter enhances:

- *Signal magnitude.* The strength of the CPD signal increases as the terrain following applied at the regions where traditional method can not provide required fly-height.
- *Signal-to-noise ratio.*
- *Resolution of measurements.* The effective area and radius of the sensor decreases as the terrain following applied, i.e. fringe field effect decreases.

Result showed that for the incline of 1.5° the terrain following technique enhances signal magnitude by 100% and narrows the response by 25% for the inner track. This has allowed recognizing features that were not visually detectable on the CPD image using usual nvCPD scanning.

An analytical model was used for nvCPD probe response. The model considered the increase in effective probe tip area from the fringe field. This modified probe response model was used to estimate the CPD probe response for the certain

experimental conditions. For the inner radius experimental results were consistent with the model calculations.

This improvement of the technique expands the application of nvCPD scanning on non-planar surfaces.

APPENDIX A

SPECIFICATION OF THE HAR-5/60 AND AS510/1

Table A.1: ELMO HAR-5/60 general specification.

FEATURE	UNIT	TECHNICAL DATA
Minimum Supply Voltage	VDC	<i>10</i>
Nominal Supply Voltage	VDC	<i>55</i>
Maximum Supply Voltage	VDC	<i>59</i>
Maximum Output Power from the Drive	W	<i>250</i>
Efficiency at Rated Power	%	<i>> 97</i>
DC (trapezoidal commutation) Continuous RMS Current limit (Ic)	A	<i>5</i>
Sinusoidal Commutation Continuous RMS Current limit (Ic)	A	<i>3.5</i>
Peak current limit (RMS)	A	<i>2 x Ic</i>
RMS output power without heatsink	%	<i>100</i>
PWM Switching Frequency	KHz	<i>22 +/-5%</i>
Switching Method		<i>Advanced Unipolar PWM</i>
Digital In / Digital Out / Analog In		<i>6 / 2 / 1</i>

Table A.2: AS510/1 general specification.

FEATURE	UNIT	TECHNICAL DATA	ADDITIONAL INFORMATION
Operating voltage	VDC	$24 \pm 20\%$ $5 \pm 5\%$	<i>reverse-polarity protection</i> <i>no reverse-polarity protection</i>
Current consumption	A	$< 75mA$	
Resolution	μm	<i>5, 10, 15, 20, 25, 50, 100</i>	<i>with quadrature evaluation DIP</i> <i>switch-selectable</i>
Output signals		<i>quadrature A, B, O</i>	<i>each inverted</i>
Real-time requirement		<i>real-time signal processing</i>	

**STEP-BY -STEP DESCRIPTION OF THE CLOSED LOOP
OPERATING DIAGRAM.**

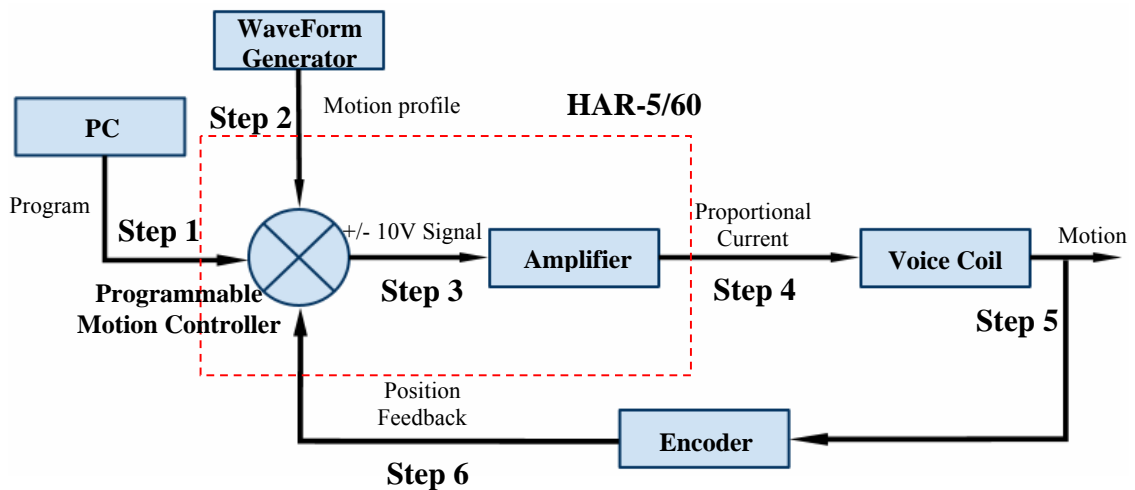


Figure A.1: Closed Loop VCA operating diagram.

Step 1: A program is written on a PC and uploaded to the motion controller. This program contains parameters and algorithm to process an input signal.

Step 2: Motion profile is sent from waveform generator to the motion controller.

Step 3: Based on the program parameters and motion profile data, the motion controller sends a +/- 10V signal to the amplifier.

Step 4: The amplifier takes the input signal and provide the necessary current to achieve the desired force from the motor.

Step 5: The motor moves to the desired position at the programmed speed and acceleration.

Step 6: Motor position is sent back to the controller to verify that the desired position has been reached and maintained.

APPENDIX B

VOICE COIL START-UP PROGRAM

```
#@AUTOEXEC           //enables automatic execution of a program at system
                      //startup

##START

#define s_R1 0.00033   //sensitivity for Range 1 of the height sensor
#define s_R2 0.00114   //sensitivity for Range 1 of the height sensor
#define resolution 0.000005 //resolution of the VCA
#define koef 64.3       //transfer coefficient
#define C -300         //constant used to move coil on safe distance
#define A 10

int n
int i
float in_offset       //analog input signal offset
float init_pos        //VCA initial position
float temp
n=0
PX=0                  //initialize position
SF =0                //smooth factor, 0 – minimal time to complete the motion
VH[3]=500            //maximum position limit
VL[3]=-500           //minimum position limit
LL[3]=-500           //low allowed motor position
HL[3]=500            //high allowed motor position
MO=1                 //enable motor
PA=0                 //defines the target position
BG                   //begin motion

i=0
in_offset = 0.0
AS[1]=0.0            //analog input offset set to 0
while (i<10)
    in_offset = in_offset + AN[1]    //read analog input at the initial position
    i = i+1
end
AS[1]=in_offset/10.0 //set up the averaged signal at initial point as offset
init_pos = AN[1]     //save the analog input value as reference point (corrected
                    //with the offset)
IL[1]=4              //digital input is used to control conditions in the next loop
```

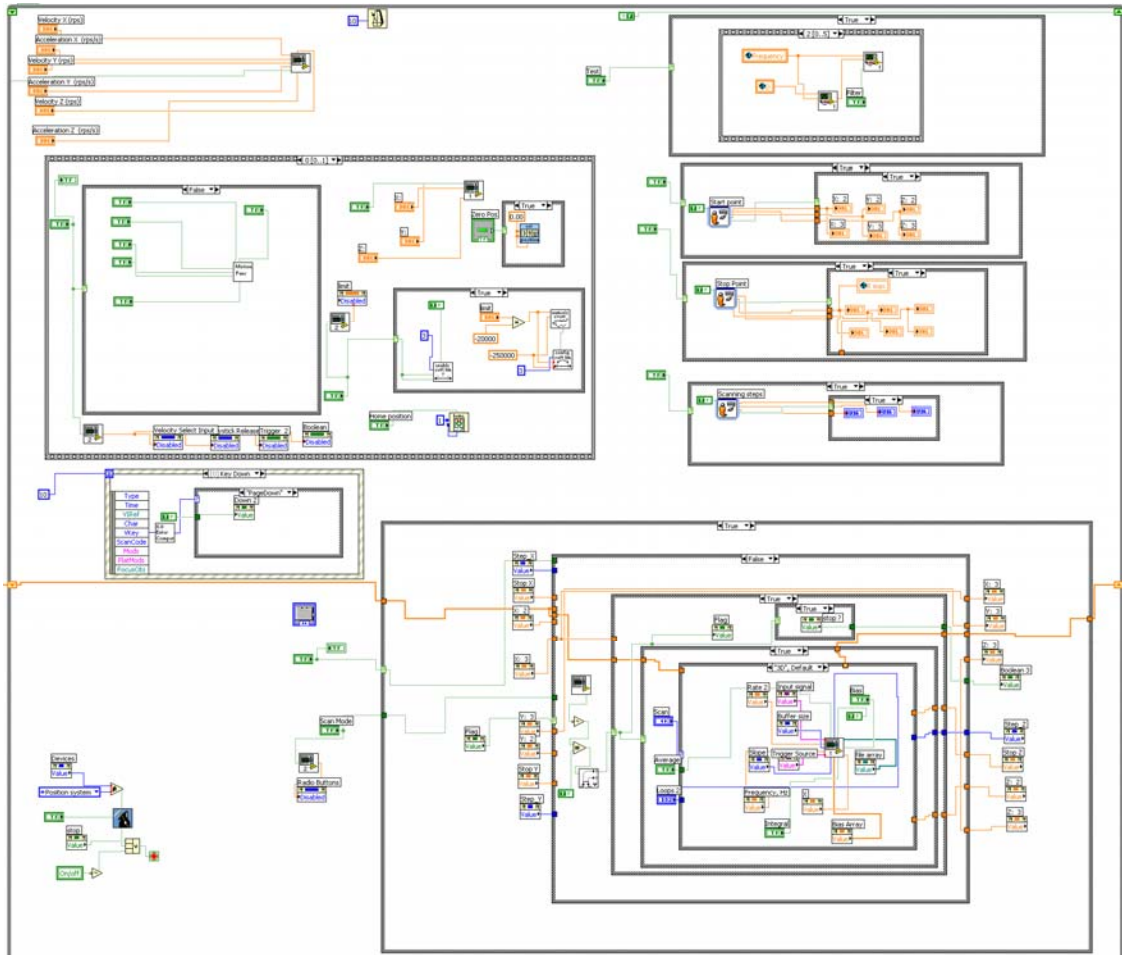
```

while(1)                                //loop that controls behavior of the VCA during scan
    temp = AN[1]-init_pos                //read analog input
    switch (IL[1])
        case 1                            //case when VCA moved up for safety purpose
            PA = C                        //absolute position is steps
        case 3                            //VCA starts following the profile at safety height
            PA = temp*koef+C              //calculate position (in steps) + safe height
        case 5                            //VCA starts following the profile at required height
            PA = temp*koef                // calculate position (in steps)
        case 7
            MO=0                          //disable motor
            return
        otherwise
            PA=init_pos*koef              //calculate initial reference position (in steps)
    end
BG                                        //begin movement
end
Exit

```

WIRE DIAGRAMS

Position System module



. Figure A.2. Wire Diagram of the position system module.

Common signal recording block

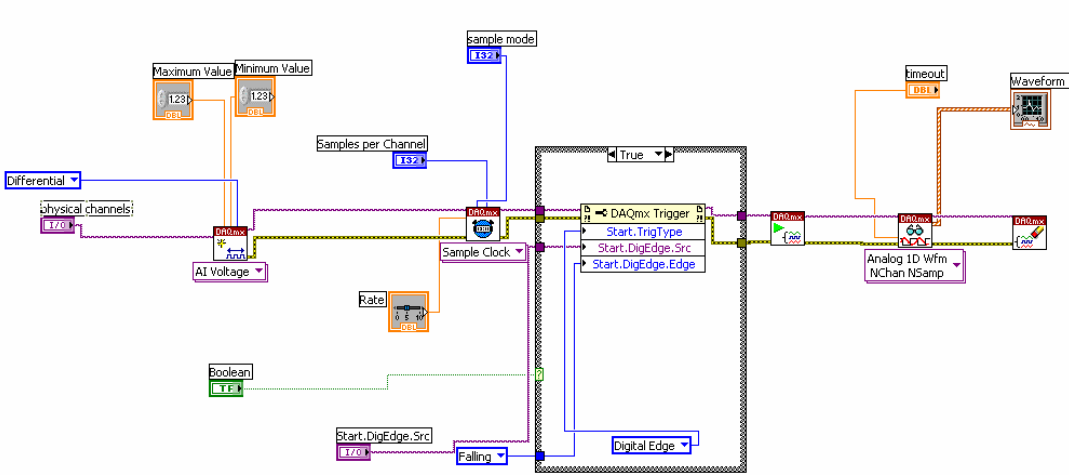


Figure A.3. Wire Diagram of a recording block.

REFERENCES

- [1] D. Yano, C. Korach, J. Streater, S. Danyluk. "Nonvibrating Contact Potential Difference Probe Measurement of a Nanometer-Scale Lubricant on a Hard Disk," *Journal of Tribology, Transactions of the ASME*, Volume 121, Issue 4, Oct 1999, p 980-983.
- [2] Y. Yang., T. Kurfess, S. Liang, S. Danyluk. "Application of a Specialized Capacitance Probe in Bearing Diagnosis", *Wear*, Volume 225-229, Part II, Apr 1999, p 1215-1221.
- [3] E. Zanoria, K. Hamall, S. Danyluk, A.L. Zharin, "The nonvibrating Kelvin probe and its application for monitoring surface wear," *Journal of Testing & Evaluation*, V. 25, No. 2, ,1997, p 233-238.
- [4] C. Yang, J. Hawthorne, B. Steele, R. Bryant, D. Sowell, D. Maloney, Katy Ip. "Inspecting Wafers Using a Potential Difference Imaging Sensor Method," *MICRO Magazine*, V.25.1, 2005.
- [5] M. Wolff, A. E. Guile, D. J. Bell. "Measurement of Localized Surface Potential Difference," *Journal of Physics E: Scientific Instruments*, V. 2, 1969, p 921-924.
- [6] I. D. Baikie, E. Venderbosch, J. A. Meyer, P. Estrup. "Analysis of Stray Capacitance in the Kelvin Method," *Review of Scientific Instruments*, V. 62, No. 3, March 1991, p 725-735.
- [7] H. Nishiyama, M. Nakamura. "Capacitance of Disk Capacitors," *IEEE Transactions on Components, Hybrids, and Manufacturing Technology*, V. 16, No. 3, May 1993, p 360-366.
- [8] A. Naini, M. Green. "Fringing fields in a parallel-plate capacitor," *American Journal of Physics*, Volume 45, Issue 9, September 1977, p 877-879.
- [9] H J Wintle. "A note on capacitors with wide electrode separation," *Journal of Physics A: Mathematical and General*, V. 25, No. 11, June 1992, L639-L642.
- [10] N. Ashcroft and N. Mermin, *Solid State Physics*. New York, 1976.

- [11] Zharin A.L. "Method of Contact Potential Difference and its Applications in Tribology", 1996
- [12] Kelvin, "Contact Electricity of Metals," Philosophical Magazine, V. 46, 1898, p 82.
- [13] W.A. Zisman, "A New Method of Measuring Contact Potential Differences in Metals," Review of Scientific Instruments, V. 3, No. 7, 1932, p367
- [14] E. Zanoria, S. Danyluk, A. Zharin, C. Bhatia, "Contact potential measurements of hard disk drive surfaces in humid environments," Journal of Vacuum Science & Technology A, V. 14 No. 1, 1996, p52-55
- [15] S. Lanyi, M. Hruskovic. "The resolution limit of scanning capacitance microscopes," Journal of Physics D: Applied Physics, V. 36, No. 5, 2003, p. 598-602.
- [16] K. Hamall, "Non Contact Measurement of Wear Induced Changes in Surface Potential," MS Thesis, Georgia Institute of Technology, Atlanta, 1996
- [17] Watt A., "Fringe Field Corrections in nvCPD Applications," MS Thesis, Georgia Institute of Technology, 2004.
- [18] W.R.Smythe, "Static and Dynamic Electricity", 2nd ed., McGraw-Hill, 1950
- [19] Landau L D, Livshits E M, "Electrodynamics of Continuous Media", Moscow: Nauka, 1982
- [20] G J Sloggett, N G Barton, S J Spencer, "Fringing fields in disc capacitors," Journal of Physics A: Mathematical and General, V. 19, No. 14, 1986, p 2725-2736.
- [21] W. C. Heerens, F. C. Vermeulen. "Capacitance of Kelvin Guard-Ring Capacitors with modified Edge Geometry," Journal of Applied Physics, V. 46, No. 6, June 1975, p 2486-2490
- [22] R Mackel, H. Baumgartner, J. Ren "The Scanning Kelvin Microscope," Review of Scientific Instruments, V. 64, No. 3, Mar 1993, p 694-699.

- [23] C.S. Korach, "Non-Vibrating Kelvin Probe Detection of Nanometer Scale Lubricant Films on a magnetic disk Surface", Master Thesis. Georgia Institute of Technology, Atlanta, GA, 1999.
- [24] Reid, Jr., Lennox Errol, "Surface Characterization of Hard Disks Using Non-Contact Work Function Capacitance Probe," Master Thesis, Georgia Institute of Technology, Atlanta, GA, 1996.
- [25] MTI Instruments. MTI-2000 User Manual.
- [26] <http://www.mtiinstruments.com/products/fiberopticmeasurement.aspx> (Accessed June 9, 2008).
- [27] National Instruments Corporation. PCI M Series User Manual, 2008.
- [28] Agilent Technologies. Agilent 33220A 20 MHz Function/Arbitrary Waveform Generator Data Sheet, 2006.
- [29] <http://www.h2wtech.com/closetoopinstructions.htm> (Accessed June, 2008).